Evolution of fluid redox in a fault zone of the Pic de Port Vieux thrust in the Pyrenees Axial Zone (Spain)

Delphine Charpentier[1], Gaétan Milesi[2], Pierre Labaume[3], Ahmed Abd Elmola[4], Martine Buatier[1], Pierre Lanari[5], and Manuel Muñoz[3]

[1]Chrono-environnement UMR6249, CNRS, Université Bourgogne Franche-Comté, 25000 Besançon, France
[2]GeoRessources, CNRS, Université de Lorraine, LabCom CREGU, 54506 Vandœuvre-lès-Nancy, France
[3]Géosciences Montpellier, CNRS, Université de Montpellier, 34095 Montpellier, France
[4]The James Hutton Institute, Environmental and Biochemical Sciences Group, Aberdeen, AB15 8QH, United Kingdom
[5]Institute of Geological Sciences, University of Bern, 3012 Bern, Switzerland

Correspondence: Delphine Charpentier (delphine.charpentier@univ-fcomte.fr)

Abstract. In mountain ranges, crustal-scale faults localize multiple episodes of deformation. It is therefore common to observe current or past geothermal systems along these structures. Understanding the fluid circulation channelized in fault zones is essential to characterize the thermochemical evolution of associated hydrothermal systems. We present a study of a palaeo-system of the Pic de Port Vieux thrust fault. This fault is a second-order thrust associated with the Gavarnie thrust in the Axial Zone of the Pyrenees. The study focused on phyllosilicates which permit the constraint of the evolution of temperature and redox of fluids at the scale of the fault system. Combined X-ray absorption near-edge structure (XANES) spectroscopy and electron probe microanalysis (EPMA) on synkinematic chlorite, closely linked to microstructural observations, were performed in both the core and damage zones of the fault zone. Regardless of the microstructural position, chlorite from the damage zone contains iron and magnesium ($Fe_{total} / (Fe_{total} + Mg)$ about 0.4), with Fe^{3+} accounting for about 30 % of the total iron. Chlorite in the core zone is enriched in total iron, but individual Fe^{3+}/Fe_{total} ratios range from 15 % to 40 %, depending on the microstructural position of the grain. Homogeneous temperature conditions about 280–290 °C have been obtained by chlorite thermometry. A scenario is proposed for the evolution of fluid–rock interaction conditions at the scale of the fault zone. It involves the circulation of a single hydrothermal fluid with homogeneous temperature but several redox properties. A highly reducing fluid evolves due to redox reactions involving progressive dissolution of hematite, accompanied by crystallization of Fe^{2+}-rich and Fe^{3+}-rich chlorite in the core zone. This study shows the importance of determining the redox state of iron in chlorite to calculate their temperature of formations and to consider the fluid evolution at the scale of a fault.

1 Introduction

Mountain ranges host a large number of deformation zones, inherited from pre-deformation events, reactivated or formed during the orogenesis and potentially active after the mountain range uplift (e.g. Dewey, 1969; Yin and Harrison, 2000; Vergés et al., 2002). In this context, faults can be characterized by the superposition of deformation events from the ductile to the brittle regime (e.g. Mitra, 1984; Holm et al., 1989; Gueydan et al., 2005; Fusseis and Handy, 2008; Rolland et al., 2009; Fossen and Cavalcante, 2017; Fossen et al., 2019; Perret et al., 2020; Kirkland et al., 2023). These fault zones typically have important associated fractures that allow channelized fluid circulation (Bense et al., 2013; Medici et al., 2023). It is therefore common to observe current or past hydrothermal circulations along these structures (Barton et al., 1995; Caine et al., 1996; Wiprut and Zoback, 2000; Mitchell and Faulkner, 2009; Faulkner et al., 2010; Belgrano et al., 2016). Luijendijk et al. (2020) highlighted the importance of the geothermal potential at the scale of mountain

ranges, such as the Alps or the North American orogens, which are essentially driven by faults. Consequently, crustal fault zones can be considered an important target for geothermal exploration (e.g. Guillou-Frottier et al., 2024), especially in an orogenic context (Diamond et al., 2018; Taillefer et al., 2018; Milesi et al., 2020; Wanner et al., 2020; Tamburello et al., 2022). In the Pyrenees (Fig. 1), several hot springs are located along major faults (Taillefer et al., 2017, 2021; Eude et al., 2020).

In the Axial Zone of the Pyrenees, shortening is marked by brittle–ductile deformation of the Paleozoic basement rocks near the unconformity with Triassic and Cretaceous units and by brittle post-orogenic events (Vissers et al., 2020; Cathelineau et al., 2021). The shortening is mainly accommodated by major thrusts (e.g. Roure et al., 1989; Muñoz, 1992; Mouthereau et al., 2014; Teixell et al., 2018; Waldner et al., 2021) which can localize active hydrothermal circulation (Vasseur et al., 1991; Jimenez et al., 2022). Several past hydrothermal records have also been described (McCaig et al., 2000; Incerpi et al., 2020; Muños-Lòpez, 2020; Cathelineau et al., 2021; Cruset et al., 2021). According to Cathelineau et al. (2021), the origin and the initial composition of the fluids in the Pyrenees may be related to important interactions with the Triassic evaporites. However, fluids evolve as they circulate and interact with the surrounding rocks. This evolution is influenced by the evolution of physical and chemical parameters and also by the evolution of the structural network. Several methods can be used to characterize the deformation events (Müller, 2003; Oriolo et al., 2018; Hueck et al., 2020; Villa, 2022; Monié et al., 2024). However, it is still difficult to distinguish the different fluid circulation events or the fluid evolution associated with the deformation (Stierman, 1984; Bruhn et al., 1994; Parry et al., 1991; Van der Pluijm et al., 2001; Morton et al., 2012; Dorsey et al., 2021) because of the lack of continuous fluid inclusion records and because the alteration products can be similar and characterized by the formation of several generations of newly formed minerals (Clauer et al., 1995; Tartaglia et al., 2020; Montemagni and Villa, 2021).

At the scale of a fault zone, the study of newly formed minerals, and in particular synkinematic phyllosilicates, allows the evolution of fluid circulation to be better constrained. Indeed, because of their layered structure and variable chemical composition, phyllosilicates are highly sensitive to pressure, temperature, and chemical ($P-T-X$) conditions, making them good candidates for recording the various fluid circulation events associated with their formation. Among them, chlorite is often observed, with different chemical compositions governed by three main substitutions (e.g. Shata and Hesse, 1998; Zane et al., 1998; Vidal et al., 2001; Lanari et al., 2014b), namely (1) the Tschermak substitution (TS), (2) the Fe^{2+}-Mg^{2+} substitution (FM), and (3) the di-trioctahedral substitution (DT).

Since chlorite generally forms in the range of 100 to 550 °C (Hayes, 1970; De Caritat et al., 1993; Walker, 1993)

in metasediments, the chemical composition is used for geothermobarometric purposes. Indeed, several chlorite thermometers have been developed (e.g. Lacroix et al., 2012; Cathelineau and Nieva, 1985; Cathelineau, 1988; De Caritat et al., 1993; Vidal et al., 2001, 2005, 2006; Inoue et al., 2009; Lanari, 2012; Bourdelle et al., 2013; Lanari et al., 2014a; see the review in Bourdelle, 2021). The chemical composition of chlorite can also be related to chemical variations during fluid circulation, especially since chlorite particles can incorporate large amounts of Fe^{3+} at low-temperature conditions. Indeed, cationic substitution can occur, implying Fe^{3+} relative to Al^{3+} or R^{2+} (Mg, Fe, Mn, and Ni) (De Grave et al., 1987; Vidal et al., 2005, 2006; Muñoz et al., 2006, 2013; Lanari et al., 2014a; Masci et al., 2019). Access to the Fe^{3+} content in chlorite allows the different chlorite populations and redox conditions of formation to be distinguished, especially when the temperature of the formation is similar.

In this work, a fault zone area with no evidence of current hydrothermal activity has been selected to investigate the main processes related to the palaeo-fluid circulation within the fault zone. The study focuses on the Pic de Port Vieux thrust (PPVT) in the Pyrenean Axial Zone, where several generations of phyllosilicates have previously been identified, dated by $^{40}Ar/^{39}Ar$, and their formation temperature has been calculated (Trincal et al., 2015, 2017; Abd Elmola et al., 2017, 2018). First, chlorite chemistry, obtained by X-ray absorption near-edge spectroscopy (XANES) and electron probe microanalysis (EPMA) on the same synkinematic minerals in clearly identified microstructures of damage and core zones was used to trace different fluid circulation events. Then, this dataset is used to refine the local mechanisms and temperature and redox conditions of fluid–rock interactions during mineral growth. Finally, a new model of fluid circulation coupled with the tectonic evolution of the PPVT is also proposed.

2 Geological setting and previous results on the Pic de Port Vieux thrust

2.1 Structural context of the Pic de Port Vieux thrust

The Axial Zone of the Pyrenees corresponds to an antiformal stack of south-dipping basement units exposing Palaeozoic rocks deformed during the Hercynian orogeny (e.g. Barnolas et al., 1996; Mouthereau et al., 2014; Cochelin et al., 2017; Teixell et al., 2018). The Pyrenees are well suited to the study of orogenic processes due to well-exposed deformation structures and exceptionally well-preserved syntectonic sedimentary rocks in the foreland (e.g. Teixell 1996). It is also an appropriate area to study the mechanisms involved in the circulation of geothermal fluids because of the important concentration of hot springs (Fig. 1).

In the southwestern part of the Pyrenean Axial Zone, the Pic de Port Vieux thrust (PPVT) is a second-order thrust
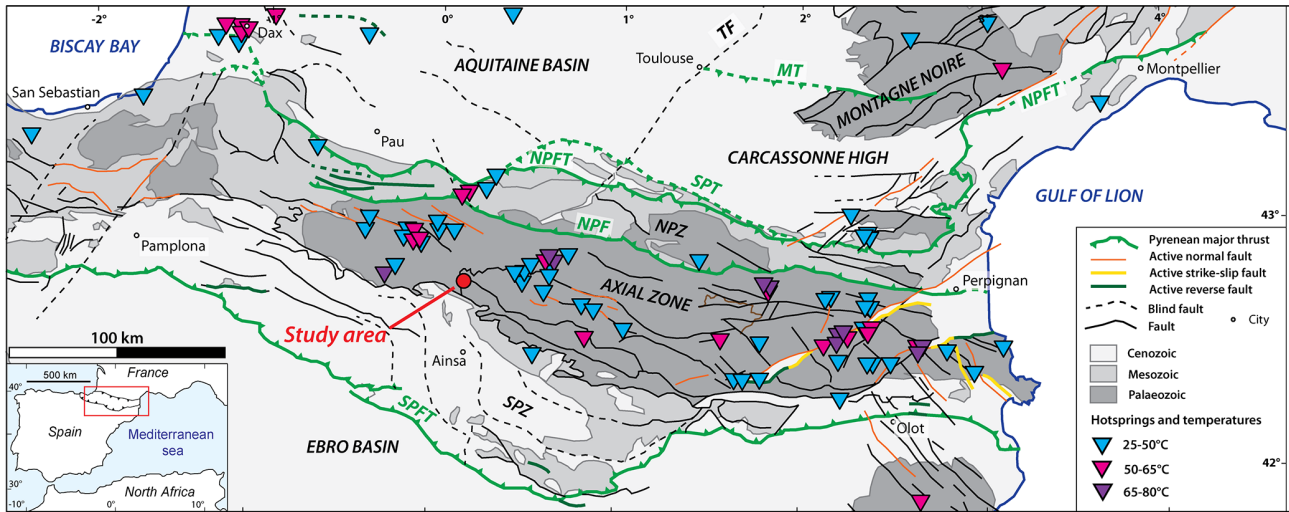
Figure 1. Structural map of the Pyrenees showing the main faults and structural domains. Current hot springs and associated temperatures are reported with coloured triangle shapes (modified after Eude et al., 2020). The study area along the Pic de Port Vieux thrust (PPVT) in the Axial Zone is indicated by a red dot.
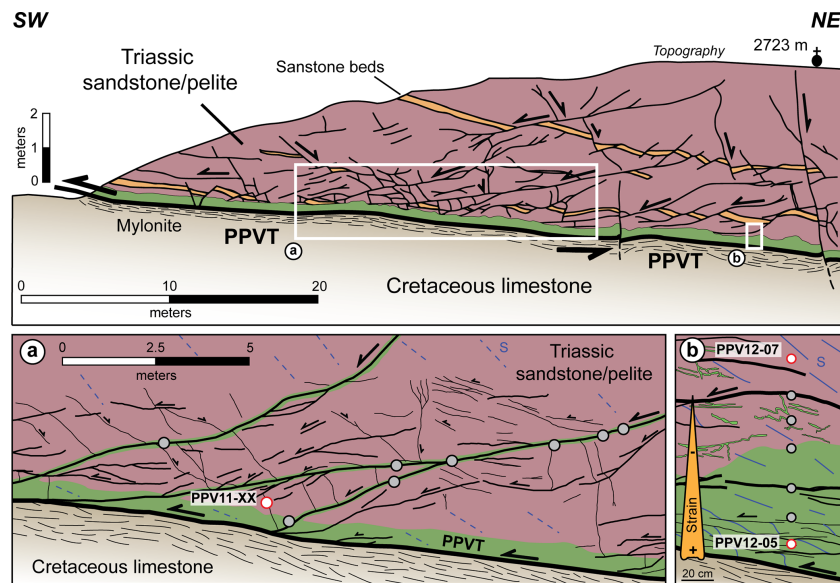

Figure 2. Pic de Port Vieux thrust (PPVT) outcrop cross section modified after Grant (1989). The PPVT superposes a hanging wall of Triassic red sandstones and pelites over a footwall of Cretaceous limestone mylonitized in the vicinity of the PPVT fault contact. The two previously studied areas (Trincal et al., 2015, 2017; Abd Elmola et al., 2017, 2018) are indicated by a white rectangle. **(a)** Focus on major synthetic normal faults underlined in green by chlorite enrichment. Samples from the study of Trincal et al. (2015) are indicated by grey dots with a black border. **(b)** Focus on a vertical transect in the PPVT fault contact with samples from the study of Abd Elmola et al. (2017, 2018). Samples studied with the X-ray absorption near-edge structure (XANES) spectroscopy method are indicated by white dots with a red border: PPV11-XX (Trincal et al., 2015), PPV12-07, and PPV12-05 (this study) from the damage zone and core zone of the PPVT, respectively.

related to the major Gavarnie thrust (Fig. 2). The latter involves a minimum southward displacement of 11.5 km of Upper Palaeozoic strata above a footwall of Lower Palaeozoic rocks and a late Variscan granite intrusion covered by Permo-Triassic and Upper Cretaceous strata (Grant, 1989). The PPVT is located in the footwall of the Gavarnie thrust

and is a late structure in relation to the Gavarnie thrust. It repeated the Triassic and Cretaceous strata with a minimum southward displacement of 0.85 km transferred to the Gavarnie thrust to the south. Deeper thrust movements then caused both regional and local folding of these earlier thrusts. ^{40}Ar/^{39}Ar radiometric studies dated the Gavarnie thrust at

36.5 ± 1.4 Ma a few kilometres SW of the PPVT (Rahl et al., 2011) and the PPVT at 36.9 ± 0.2 Ma (Abd Elmola et al., 2018). The Triassic strata comprise a predominantly mudstone sequence with thin interbedded fining-upward sandstone units; the Cretaceous strata are constituted by limestone (Grant, 1990).

2.2 Macroscopic structure of the Pic de Port Vieux thrust

Structural analysis of the PPVT reveals a multi-phase tectonic history with several stages of deformation, the structures and microstructures of which have been extensively studied by Grant (1989, 1990, 1992) and Grant et al. (1990). On the studied outcrop, located a few tens of metres below the Gavarnie thrust, the PPVT fault is subhorizontal and overlies a hanging wall of Lower Triassic red pelites and sandstones with intercalation of thin yellowish dolomitic carbonate beds over a footwall of Upper Cretaceous carbonates (Figs. 2 and 3a, b). In the footwall, the fault zone consists of dolomitic limestone that is progressively transformed into mylonitic limestone near the fault contact with a fault-parallel foliation (Fig. 3a–d). In the hanging wall, the fault core, a few decimetres thick, is characterized by an intense S–C structure in pelites associated with quartz and chlorite veins (Fig. 3c and d). The S–C asymmetry and centimetre-scale micro-folds indicate top–south shearing. Above, the damage zone is characterized by moderate north-dipping beds affected by a complex network of secondary faults and associated quartz and chlorite veins, as well as a slaty schistosity in the pelite. Grant (1992) distinguished seven stages of deformation with (1) pre-thrusting normal faults; (2) fault rotation and cleavage formation associated with the emplacement of the overlying Gavarnie thrust; (3–4) bedding-parallel slip synthetic to the thrust (Fig. 3e), followed by antithetic steep-dip normal faults (X-shears in the Riedel terminology; AF in Fig. 3a and b) during thrusting; (5) synthetic and antithetic normal faults cutting the thrust; (6) synthetic low-dip normal faults branching on the thrust (R shears; SF in Fig. 3a, b, e, and f); and (7) local thrust reactivation during folding due to emplacement of underlying thrusts. The synthetic normal faults of stage 6 rotated the stratigraphy to its present north-dipping orientation. They are interpreted by Grant (1992) as indicative of thrust reactivation by late gravity spreading/gliding. Schistosity in the pelite has a northward dip oblique to the bedding in the Triassic footwall (Grant, 1989), but in the lower part of the damage zone studied here, the northward dip is subparallel to the rotated bedding characterized by sandstone beds and thin carbonate beds. In the sandstone, bedding-parallel stylolites are also observed (Fig. 3f and h).

Quartz and chlorite veins are associated with the various stages of deformation, attesting to the strong involvement of fluids in the deformation (Grant, 1989, 1992; Grant et al., 1990; Trincal et al., 2015, 2017). They can occur as isolated tension gashes with different dips, including veins parallel to the schistosity (V in Fig. 3d and f), en echelon arrays (Fig. 3a, e, g, and h), or fibrous coatings on fault surfaces (Fig. 3g). Another fluid-related distinctive feature of the hanging wall fault zone is the greenish colour of the first few decimetres above the thrust surface, corresponding to the core zone and lower part of the damage zone (Fig. 3a and b), while the overlying strata retain the original red colour, except along the main faults, particularly the synthetic normal faults, where the greenish colour is also present (Figs. 2 and 3e, f). Fluid inclusion analyses (Grant, 1990; McCaig et al., 1995; Trittla et al., 2000), calcite isotopic analyses (Trincal et al., 2017), and geochemical modelling of mineralogical transformations (Abd Elmola et al., 2017) indicated that the formation of the veins could be contemporaneous with the bleaching by highly reducing fluids derived from the evaporitic Triassic (Cathelineau et al., 2021).

2.3 Chlorite occurrences and estimated formation temperatures

Chlorite is as a sensitive proxy for fluid properties and chemistry. Chlorite from the PPVT outcrop (Fig. 2) was first described by Grant (1989). Subsequently, Trincal et al. (2015) and Abd Elmola et al. (2017) studied samples whose localization is shown in Fig. 2a and b.

In the damage zone, chlorite is frequently observed in the matrix as elongated large grains (50 µm), suggesting a detrital origin, and it occasionally appears as diagenetic stacks associated with white mica (Abd Elmola et al., 2017). In both the damage zone and the core zone, synkinematic chlorites are observed within extensional and shear quartz–chlorite veins.

In most veins, chlorite has a linear texture. Chlorite crystals are preferentially developed along the vein–host rock interface and quartz crystals occur as elongated crystals with the axis perpendicular to the vein boundaries. When a vein crosses alternating pelitic and sandy layers, chlorite is preferentially concentrated along the pelitic layers (Trincal et al., 2015). The chemical composition of the chlorite is homogeneous. The only difference observed between the various synkinematic chlorite generations is that near the fault contact, newly formed chlorite is enriched in Fe compared to newly formed chlorite from the damage zone (Abd Elmola et al., 2017). Their average formation temperature was estimated using chlorite thermometry to be 270 ± 23 °C for the damage zone and 285 ± 28 °C for the core zone.

In open cavities along shear veins, chlorite occurs as pseudo-uniaxial plates arranged in rosette-shaped aggregates that appear to have formed as a result of radial growth (Trincal et al., 2015). The chlorite rosettes have discrete growth zones due to variations in the FeO and MgO content. This chemical zonation was interpreted to be the result of a series of heating and cooling cycles between 300 and 400 °C during crystallization (Trincal et al., 2015).
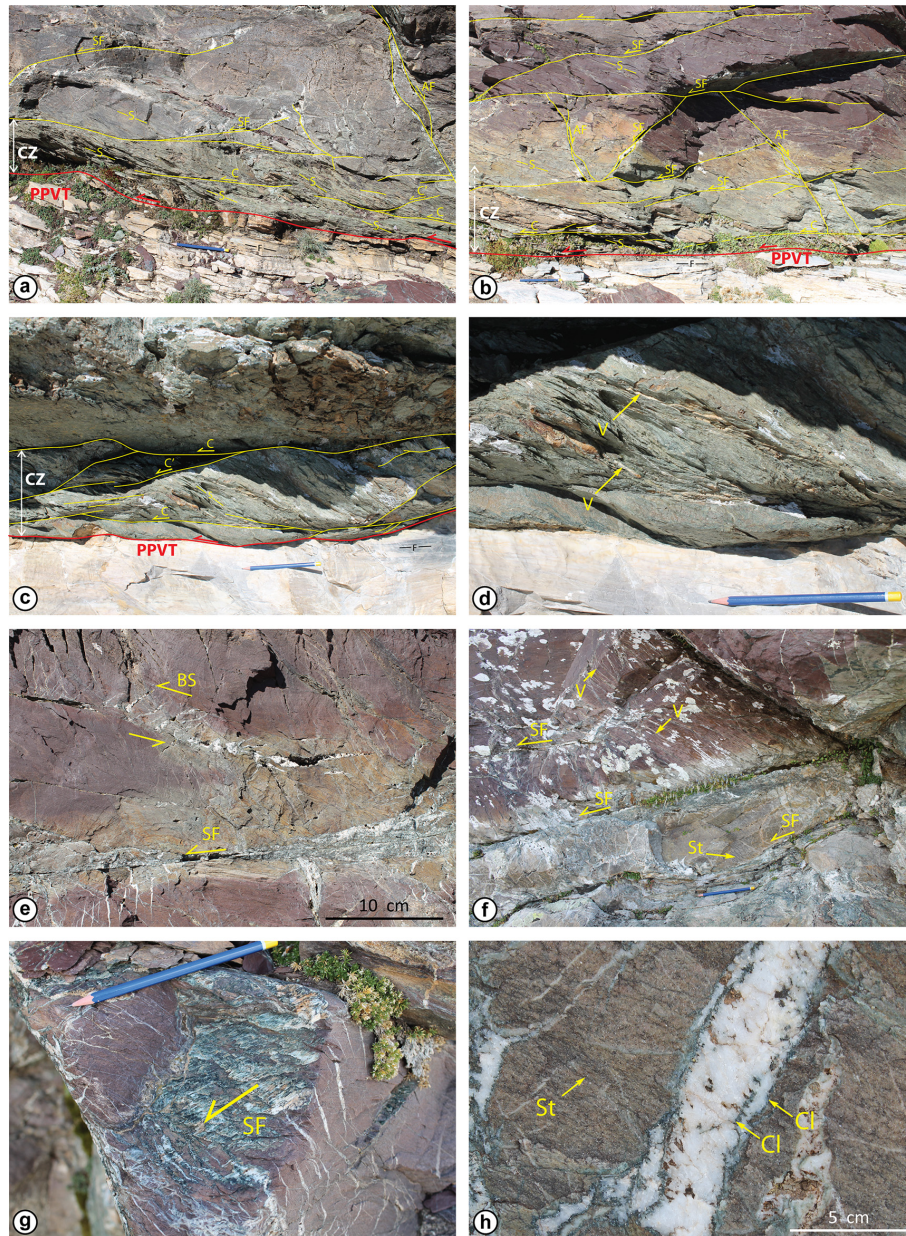
Figure 3. Field pictures of the Pic de Port Vieux thrust fault zone. **(a, b)** General view of the thrust fault zone comprising Upper Cretaceous foliated carbonate in the footwall and Lower Triassic pelite and sandstone in the hanging wall. The latter features a decimetre thick core zone with an intense S–C structure and a damage zone with bedding-parallel schistosity and a complex network of veins and secondary faults. Note the greenish colour of the hanging wall core zone and the lower part of damage zone passing upward to the original red colour of the Triassic sediment. **(c)** Detailed view of the thrust surface with footwall foliated carbonate and hanging wall core zone with the S–C structure in pelite. **(d)** Details of C, showing quartz veins along schistosity surfaces. **(e)** Detailed view of synthetic normal faults and associated veins in the hanging wall damage zone. Note the greenish colour around the main deformation zones, while the original red colour of the Triassic sediment is preserved elsewhere. **(f)** Detailed view of secondary faults, schistosity-parallel veins in pelite (upper part), and bedding-parallel stylolites in sandstone (lower part) in the hanging wall damage zone. In the pelite, note the greenish colour along the fault surface while the original red colour is preserved above. **(g)** Detailed view of the surface of a synthetic normal fault in the hanging wall damage zone featuring coating of fibrous quartz (white) and chlorite (green). **(h)** Detailed view of an extensional vein in sandstone of the hanging wall damage zone with quartz filling (white) and a concentration of chlorite along vein walls or in parallel wall bands (green). Bedding-parallel stylolites are present in sandstone. All deformation features shown in these pictures are compatible with top south (left on all pictures) shearing, with the bedding being rotated by low-angle normal faults synthetic to the main thrust. See comments in the text. AF is the antithetic normal fault; BS is the en echelon vein array marking the bedding-slip synthetic to the main thrust; C, C′, is the shear surfaces in S–C structure; CZ is the core zone; F is the foliation in the footwall carbonates; PPVT is the Pic de Port Vieux thrust surface; S is the schistosity; SF is the synthetic normal fault; St is the stylolite; and V is the schistosity-parallel vein.

According to the previous temperature studies on the PPVT, the fault activity occurred under low-grade metamorphic conditions (greenschist facies). The mylonitization of footwall carbonates associated with the fault activity was estimated by Raman spectroscopy of carbonaceous material around 300 °C (Trincal et al., 2017). Calculation of chlorite formation temperatures indicates a wide range of temperature conditions around 250–300 °C (Abd Elmola et al., 2017) or around 300–400 °C (Trincal et al., 2015) for chlorite formation in the hanging wall. In this paper, the quantification of $XFe^{3+} = Fe^{3+}/Fe_{total}$ in synkinematic chlorite is used to refine formation temperature (see Sect. 5).

3 Sampling and analytical techniques

3.1 Sampling

Based on the previous detailed studies of the pelite samples from a vertical transect in the PPVT hanging wall fault zone (Trincal et al., 2015, 2017; Abd Elmola et al., 2017), two representative samples were selected for the present study (Fig. 2b). These two samples are also the two samples used by Abd Elmola et al. (2018) to date the K white mica. In the damage zone, sample PPV12-07 is located in the red pelites about 1.5 m away from the fault contact. In the core zone, sample PPV12-05 is located a few centimetres away from the fault contact. The GPS coordinates for the two sample locations are 42°43′40.52″ N and 0°9′44.67″ E.

3.2 Petrographic observations

Petrographic observations were carried out at the FEMTO-ST Institute (University of Franche-Comté). Microstructures and mineral assemblages were analysed using a JEOL JSM5600 instrument (scanning electron microscope, SEM) equipped with secondary electron (SE), backscatter secondary electron (BSE), and energy dispersive X-ray spectroscopy (EDX) detectors.

3.3 Chemical analyses

Quantitative chemical analyses of chlorite were performed using an electron probe microanalyser (EPMA) JEOL 8200 at the Institute of Geological Sciences (University of Bern). The following natural and synthetic standards were used: orthoclase (SiO_2, K_2O), anorthite (Al_2O_3, CaO) albite (Na_2O), almandine (FeO), forsterite (MgO), tephroite (MnO), and ilmenite (TiO_2). Analyses were carried out at 15 keV accelerating voltage, 10 nA specimen current, and 40 s dwell time (including 2×10 s of background measurement).

3.4 Iron oxidation state

To characterize the distribution and determine, in situ, the oxidation state of iron in chlorite crystals, X-ray fluorescence (XRF) and Fe K-edge XANES data were, respectively, collected at the BM23 beamline of the European Synchrotron Radiation Facility (ESRF; Grenoble, France) using the micro-focused experimental setup (Mathon et al., 2015). The storage ring was operated in the 16-bunch mode with an average current of 75 mA, which is suitable for this type of redox measurement, while avoiding beam damage. X-rays were generated using a bending magnet and monochromatized using a double-crystal fixed exit Si(111) monochromator. Micro-focusing mirrors arranged in the KB (Kirkpatrick–Baez) geometry were used to focus the beam down to ~ 4 mm $\times$ 4 mm FWHM (full-width half maximum). Data were collected in fluorescence mode using a Vortex silicon drift diode positioned at 85° to the incident X-ray beam. Samples were positioned perpendicular to the X-ray beam to minimize self-absorption (Pfalzer et al., 1999). XRF maps were first recorded at 9 keV with a spatial resolution of 10 μm and a dwell time of 0.5 s. The μ-XANES spectra (Fig. S1 in the Supplement) were collected at the Fe K edge for different positions on the XRF maps. Data normalization and pre-peak fits were performed using the XASMAP package, which was originally designed for dispersive μ-XANES mapping applications (see Fe–chlorite study in Muñoz et al., 2006). The Fe K edges were fitted between 7108 and 7118 eV using three pseudo-Voigt functions, following the procedure described in Muñoz et al. (2013). To derive the iron speciation, the pre-edge calibration was based on the following powder standards: staurolite ($^{[IV]}Fe^{2+}$), siderite ($^{[VI]}Fe^{2+}$), andradite ($^{[VI]}Fe^{3+}$), and sanidine ($^{[IV]}Fe^{3+}$), according to Wilke et al. (2001). Chlorite crystals were oriented in the magic angle geometry to avoid polarization effects in the XANES and pre-edge regions (i.e. crystal orientation relative to the polarized X-ray beam), in agreement with Muñoz et al. (2013).

3.5 Chlorite thermometry

In the current study, chlorite crystallization temperatures have been estimated using the microprobe analyses coupled with the μ-XANES Fe speciation analyses. This coupling allows us to consider the real amount of Fe^{3+}. Indeed, at low-temperature conditions, chlorite incorporates large amounts of Fe^{3+} (up to 50 % of the total Fe; Vidal et al., 2005; Lanari et al., 2014a). However, the cationic substitution implying Fe^{3+} relative to Al or R^{2+} (Mg, Fe, Mn, Ni, etc.) is rarely constrained. This is due to the difficulty in accurately measuring the number of Fe^{3+} cations present in the crystal structure and their location on the crystallographic sites. But it is important to consider the amount of Fe^{3+} as it can reduce the R^{2+} occupancy and increase the number of octahedral vacancies (e.g. Vidal et al., 2005). As the octahedral vacancy is correlated with temperature (e.g. Lanari et al., 2014a), the reduced R^{2+} occupancy can result in a lower calculated temperature. The temperature variation caused by the introduction of Fe^{3+} content is different for each thermome-

ter (e.g. Inoue et al., 2009, and references therein; Bourdelle et al., 2013; Vidal et al., 2016).

Since the analyses of newly formed chlorite from both the damage and the core zones can be expressed using the clinochlore, daphnite, Mg sudoite, and amesite end-members (see Sect. 4 below), temperatures were estimated by multi-equilibrium thermodynamic calculations using the method and solid solution models of Vidal et al. (2005, 2006). This method is based on thermodynamic calculations of equilibrium conditions for chlorite, the composition of which is expressed as the activities of end-member components with known thermodynamic properties and solution models (Berman, 1991; Vidal et al., 2001); the XFe^{3+} ratio $(XFe^{3+} = Fe^{3+}/(Fe^{3+} + Fe^{2+}))$ is optimized in the chlorite calculation to satisfy the convergence criteria. The estimated XFe^{3+} values were compared to the XFe^{3+} values measured by μ-XANES.

Additionally, temperatures were calculated using the ChlMicaEqui program of Lanari et al. (2014a) and using the method of Vidal et al. (2005) with a fixed XFe^{3+} ratio corresponding to the μ-XANES results. The semi-empirical thermometer developed by Inoue et al. (2009) was also applied because it was developed for low-temperature chlorite with known XFe^{3+} contents. Results from previous studies such as Abd Elmola et al. (2017) were integrated in the discussion.

4 Results

4.1 Petrography and microstructures

The petrography and microstructure of the two studied samples are shown in Figs. 4–6.

The damage zone sample PPV12-07, located in the hanging wall approximately 1.5 m above the fault contact, is composed mainly of a red pelitic matrix (Fig. 4a). At the micrometre scale, the schistosity corresponds to the preferred orientation of elongated grains of quartz and phyllosilicates (S in Figs. 4a–c and 5a, d). In the mineral matrix, chlorite occurs as elongated large grains (50 μm), suggesting a detrital origin. The sample also contains two main generations of veins. The first generation corresponds to quartz veins parallel to the schistosity with abundant oxide patches (V1 in Fig. 4a–c). No clear shear criteria are observed in these veins, suggesting an extensional opening perpendicular to the schistosity. The second generation of veins corresponds to quartz and chlorite veins associated with the extensional deformation of the schistosity and previous veins (V2 in Fig. 4a–c). They occur (i) in extensional openings corresponding to boudinage of the V1 veins (1 in Fig. 4b), (ii) as a coating along the edges of V1 veins (2 in Fig. 4b and c), and (iii) in releasing oversteps zones associated with shear surfaces that are extensional with respect to schistosity (V2 in Fig. 4c).

Synkinematic chlorites were analysed in areas labelled 1 and 2 in Fig. 4a and illustrated in Fig. 5. Area 1 corresponds to a releasing overstep zone between shear surfaces where optical and SEM images show a strong imbrication of chlorite and quartz grains (Fig. 5a–c). This texture indicates a simultaneous formation of these two phases. The chlorite grains are straight particles ranging from a few microns to a few tens of microns (Fig. 5c). Area 2 is an extensional vein at a high angle to the schistosity and with a sigmoidal geometry that is also compatible with the release of overstep opening zones between shear surfaces. In this vein, chlorite is mainly located at the vein margins with quartz in the centre of the vein (Fig. 5d and e). Chlorite aggregates are composed of elongated crystals (Fig. 5f).

The core zone sample PPV12-05, located a few centimetres away from the fault contact, consists of greenish pelite with strongly developed schistosity (Fig. 4d and e). Compared to the damage zone sample, quartz grains are less abundant, smaller, and have more elongated shapes aligned with the schistosity. The schistosity is deformed by S–C shear structures and micro-folds consistent with those observed macroscopically (Fig. 3c and d), both indicative of top to south shearing. The same schistosity-parallel V1 quartz veins as in the damage zone sample are abundant, and they are also affected by boudinage, with boudins separated by extensional openings or shear planes (B and C' in Fig. 4d, respectively), consistent with schistosity-parallel extension. High-angle extensional fractures are also common across the V1 veins. Intense shear deformation is also indicated by partial mylonitization of the V1 veins (Fig. 4e). Quartz + chlorite precipitated in the interboudin domains, in high-angle extension fractures across the V1 veins, and as coatings along the margins of the V1, which is similar to the damage zone sample, but also in mylonitized shear bands in the V1 veins (Fig. 4f). On the other hand, in contrast to sample PPV12-07, there is no quartz + chlorite vein in releasing oversteps zones along oblique shear surfaces.

Synkinematic chlorites were analysed in domains labelled Area 1 and Area 2 in Fig. 4d and shown in Fig. 6. Area 1 corresponds to an interboudin domain with disoriented chlorite grains associated with rare small quartz grains (Fig. 6a–c). Chlorite from Area 2 is located at the margin of a V1 quartz vein that also contains chlorite in mylonitized corridors (Fig. 6d–f). Chlorite shows an elongated grain shape and is imbricated with quartz grains at the contact with the V1 vein, while chlorite is associated with newly formed white mica at the boundary with the matrix (Fig. 6e and f).

The EPMA analyses were carried out in each area (red dots in Figs. 5 and 6), and the chlorite compositions are given in Table S1 in the Supplement. The XANES data were also obtained in each area, and their localization is shown by blue points in Figs. 5 and 6. The energy position of the centroid, its intensity, and the corresponding Fe^{3+}/Fe_{total} ratio for each pre-edge peak are given in Table S2.
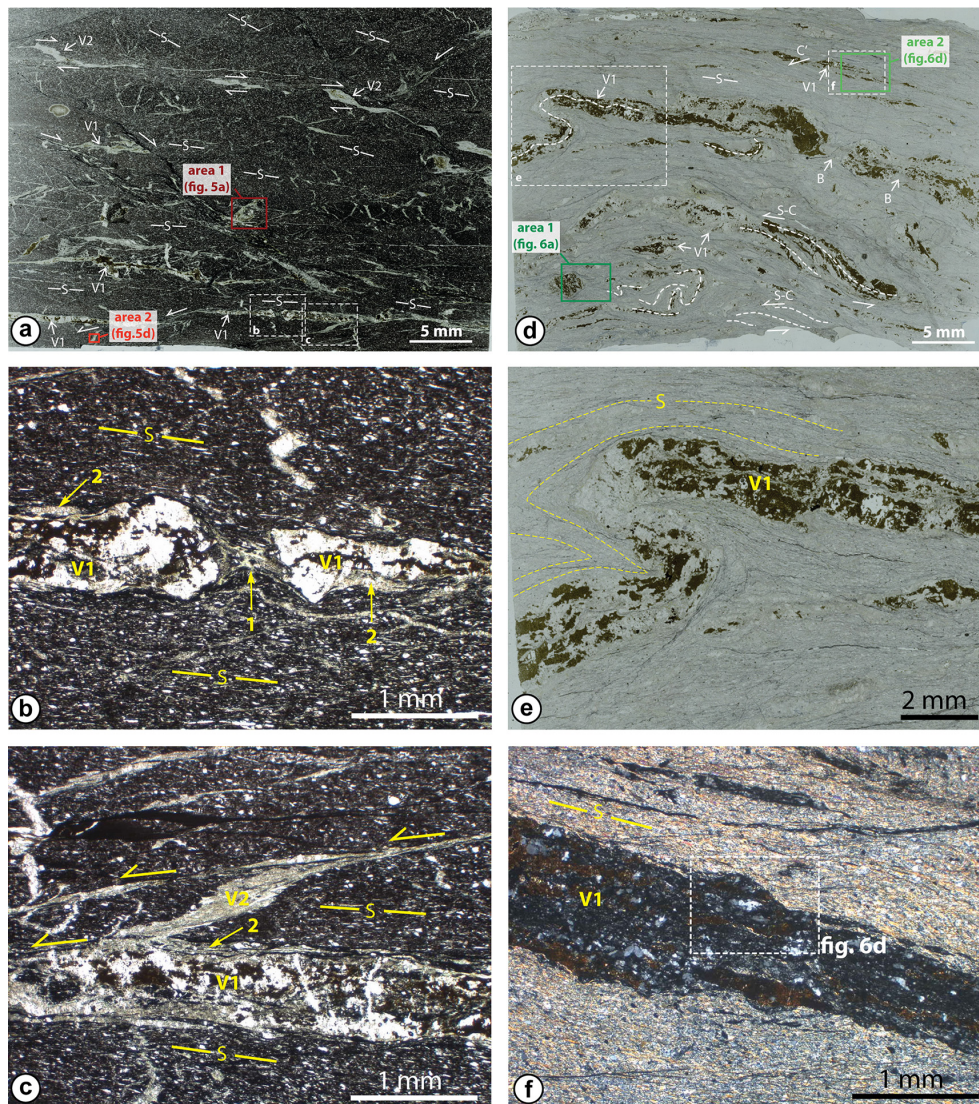
Figure 4. Scan images of the studied thin sections in the Triassic rocks of the thrust fault hanging wall showing detail of microstructures. **(a–c)** PPV12-07 sample from the damage zone. **(a)** Early schistosity-parallel quartz veins featuring iron oxide patches are stretched by boudinage and cross-cut by younger shear surfaces (arrows). A second generation of quartz–chlorite veins occurs in releasing oversteps along shear surfaces. **(b)** Boudinage of an early schistosity-parallel quartz vein with iron oxide patches with quartz + chlorite precipitation in the interboudin and along the early vein. **(c)** Late quartz + chlorite vein in a releasing overstep along shear surfaces (arrows) and quartz + chlorite precipitation along the early vein. **(d–f)** PPV12-05 sample from the core zone. The same early schistosity-parallel veins as in panel **(a)** are stretched by boudinage, folded, and involved, together with schistosity, in S–C shear structures. Fold asymmetry and S–C structures indicate top to left (south) shearing C. Folded early schistosity-parallel quartz vein. **(d)** Early vein with mylonitized quartz fill. **(e)** Quartz + chlorite precipitated in interboudin opening. **(f)** Quartz + chlorite precipitated along early quartz vein. Frames localize detailed pictures in Figs. 5 and 6. B is for boudinage; C, C′, is for shear surfaces; S is for schistosity; V1 is for early schistosity-parallel quartz veins; and V2 is for younger quartz + chlorite veins in releasing oversteps along shear surfaces.

4.2 Estimation of iron speciation from XANES spectra

The results in terms of the integrated area and centroid energy positions are presented in a variogram (Fig. 7). The accuracy of the centroid value is estimated to be $\pm 0.05\,\mathrm{eV}$ (Muñoz et al., 2013). This variogram also shows the reference values obtained for the standard reference materials (white circles) used to calibrate the data (see Wilke et al., 2001, for details).

The results are distributed between the two $^{[VI]}\mathrm{Fe}^{2+}$ and $^{[VI]}\mathrm{Fe}^{3+}$ end-members, implying that all iron cations of the measured chlorite are located in the octahedral sites. The centroid energy values obtained for Area 1 and Area 2 of the damage zone (sample PV12-07) are homogeneous around
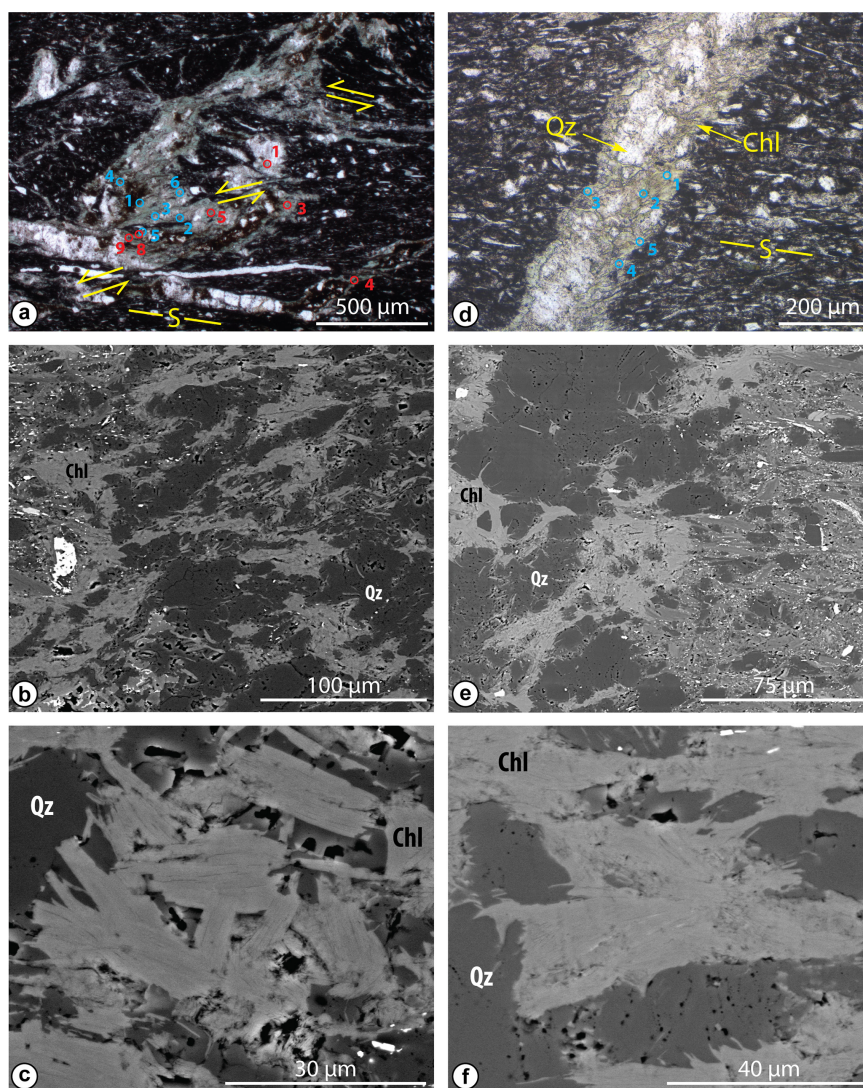
Figure 5. Location of analyses on the PPV12-07 sample from the damage zone. **(a–c)** Area 1 in Fig. 4a. **(a)** Optical microscope picture of the analysed area with location of analyses in a quartz + chlorite vein in a releasing overstep between shear surfaces (arrows). The location of the μ-XANES analyses is in blue, and the microprobe analyses are in red. **(b)** SEM image showing the strong imbrication of chlorite particles and quartz grains. **(c)** Details of chlorite particles morphology. **(d–f)** Area 2 in Fig. 4a. **(d)** Optical microscope picture of the analysed quartz + chlorite vein. The location of the μ-XANES analyses is in blue. **(e)** SEM image showing that chlorite particles are mainly located on the edges of the vein, while quartz is in the centre. **(f)** Details of chlorite particle morphology. Ch is for chlorite, Qz is for quartz, and S is for schistosity.

7113.5 eV. For the core zone (sample PV12-05), the chlorite has different values in the two areas analysed. The values for chlorite from Area 1 are broadly similar to those for chlorite from Area 1 and Area 2 in the damage zone (sample PV12-07), whereas chlorite from Area 2 has smaller centroid energy values. The calibration to XFe^{3+} is shown in Table S2. The proportions of Fe^{3+} in chlorite from each area are relatively homogeneous, allowing average values to be calculated. In both areas of sample PPV12-07, XFe^{3+} is of 31 and $32 \pm 5\%$. The proportion is higher ($39 \pm 9\%$) in chlorite from Area 1 of the core zone (sample PV12-05) and much

lower ($16 \pm 7\%$) in chlorite from Area 2 of the core zone (sample PV12-05).

4.3 Chlorite compositions

μ-XANES and microprobe results were coupled to calculate the structural formulae of newly formed chlorite (Table S3). For each area, the chlorite composition is very homogeneous, allowing average structural formula calculation. Structural formulae were calculated on a 14 oxygens basis, considering the average XFe^{3+} value. $[Si_{2.78}Al_{1.22}O_{10}]$ $(Al_{1.52}Fe^{3+}_{0.54}Fe^{2+}_{1.19}Mg_{2.58}\square_{0.16})$ $(OH)_8$ and
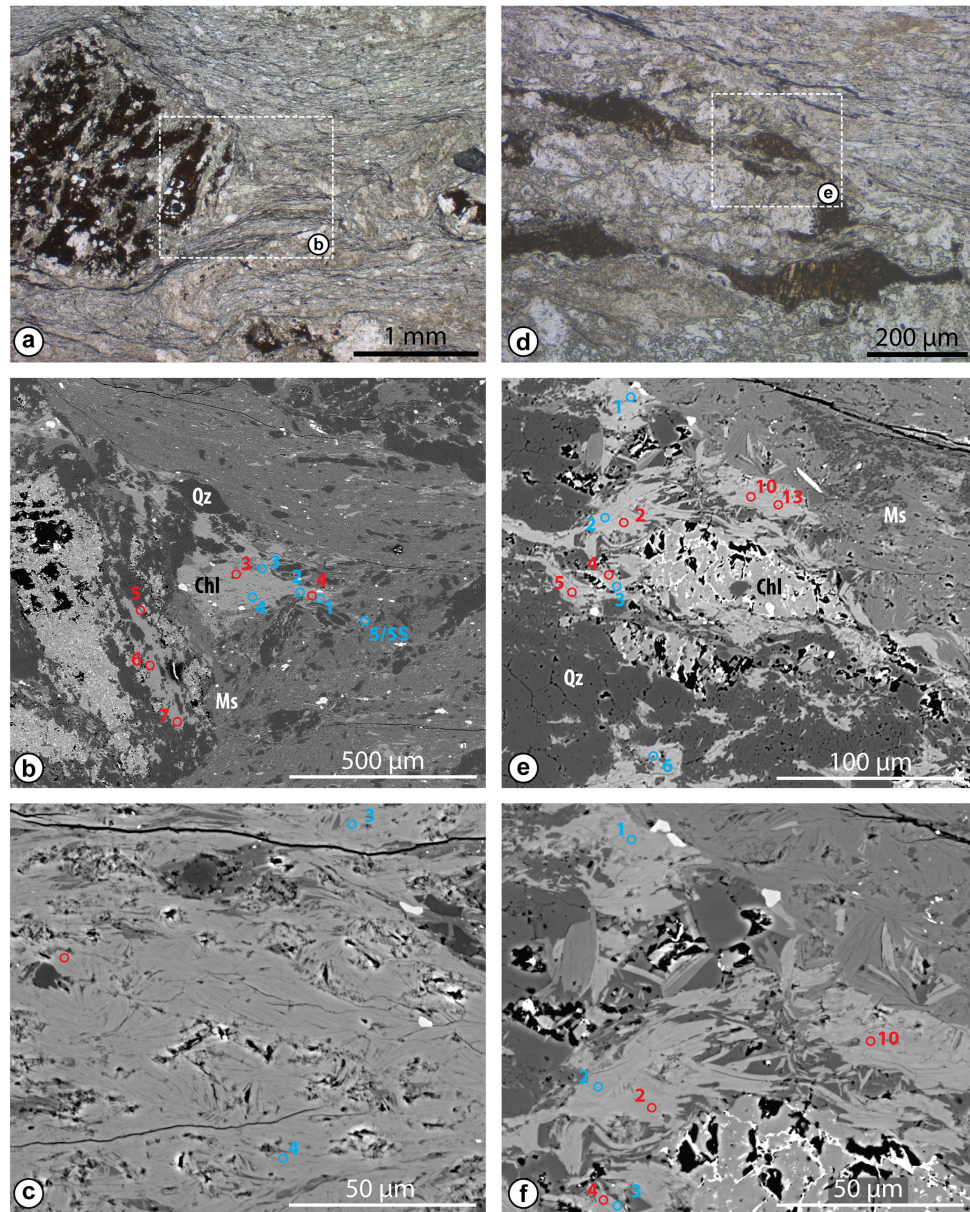
Figure 6. Location of analyses on the PPV12-05 sample from the core zone. **(a–c)** Area 1 in Fig. 4d. **(a)** Thin-section scan image showing boudinage and schistosity-parallel quartz vein with oxide patches. Quartz + chlorite precipitated in the interboudin opening and in high-angle extension veins across the early quartz vein. **(b)** SEM image showing chlorite in the strain shadow at the edge of the boudinage opening (see frame in panel **a**). The location of the μ-XANES analyses is in blue, and the microprobe analyses are in red. **(c)** Details of the chlorite particle morphology. **(d–f)** Area 2 in Fig. 4d. **(d)** Optical microscope image showing an early schistosity-parallel quartz vein deformed by shear bands with mylonitized quartz and chlorite precipitation. **(e)** SEM image showing chlorite located at the edge of a shear vein of quartz + chlorite (cf. frame in panel **d**). The location of the μ-XANES analyses is in blue, and the microprobe analyses are in red. **(f)** Details of chlorite particle morphology. Elongated chlorite particles are imbricated with quartz grains.

$[Si_{2.77}Al_{1.23}O_{10}]$ $(Al_{1.52}Fe^{3+}_{0.55}Fe^{2+}_{1.17}Mg_{2.60}\square_{0.15})$ $(OH)_8$ are average structural formulae for newly formed chlorite from the damage zone in Area 1 and Area 2, respectively. $[Si_{2.78}Al_{1.22}O_{10}]$ $(Al_{1.51}Fe^{3+}_{0.77}Fe^{2+}_{1.20}Mg_{2.37}\square_{0.15})$ $(OH)_8$ and $[Si_{2.77}Al_{1.23}O_{10}]$ $(Al_{1.54}Fe^{3+}_{0.31}Fe^{2+}_{1.61}Mg_{2.36}\square_{0.17})$ $(OH)_8$ are average structural formulae for newly formed

chlorites from the core zone in Area 1 and Area 2, respectively.

Structural formula values were then plotted on Si vs. R^{2+}, R^{3+} vs. R^{2+}, Si vs. $Fe_{total}/(Fe_{total} + Mg)$, and Fe^{3+} vs. ^{VI}Al diagrams (Fig. 8). Newly formed chlorite from both the damage and the core zones lies between the clinochlore–
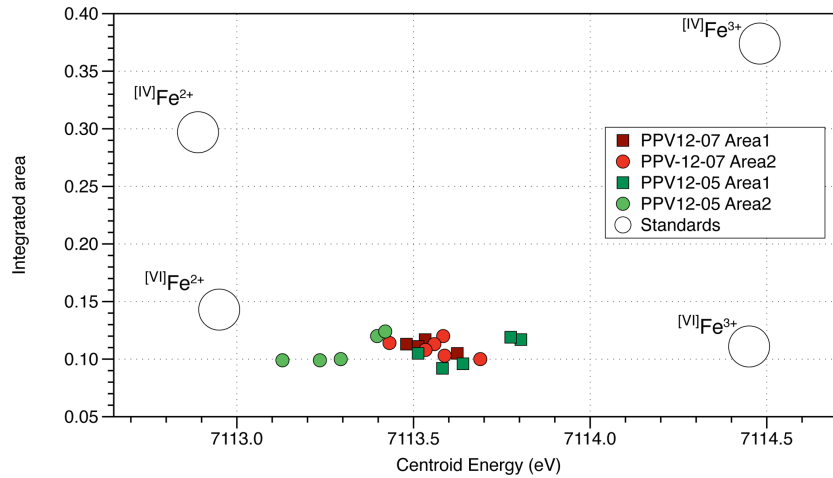
Figure 7. Integrated area versus centroid position variogram showing the positions of the standards (andradite for $^{[VI]}Fe^{3+}$, sanidine for $^{[IV]}Fe^{3+}$, staurolite for $^{[IV]}Fe^{2+}$, and siderite for $^{[VI]}Fe^{2+}$), together with the data from chlorite particles from the damage zone in red (sample PPV12-07) and from the core zone in green (sample PPV12-05), with squares for Area 1 and circles for Area 2 (cf. Figs. 5 and 6 for analyses location). $^{[VI]}Fe$ is for iron in octahedral sheets. $^{[IV]}Fe$ is for iron in tetrahedral sheets.
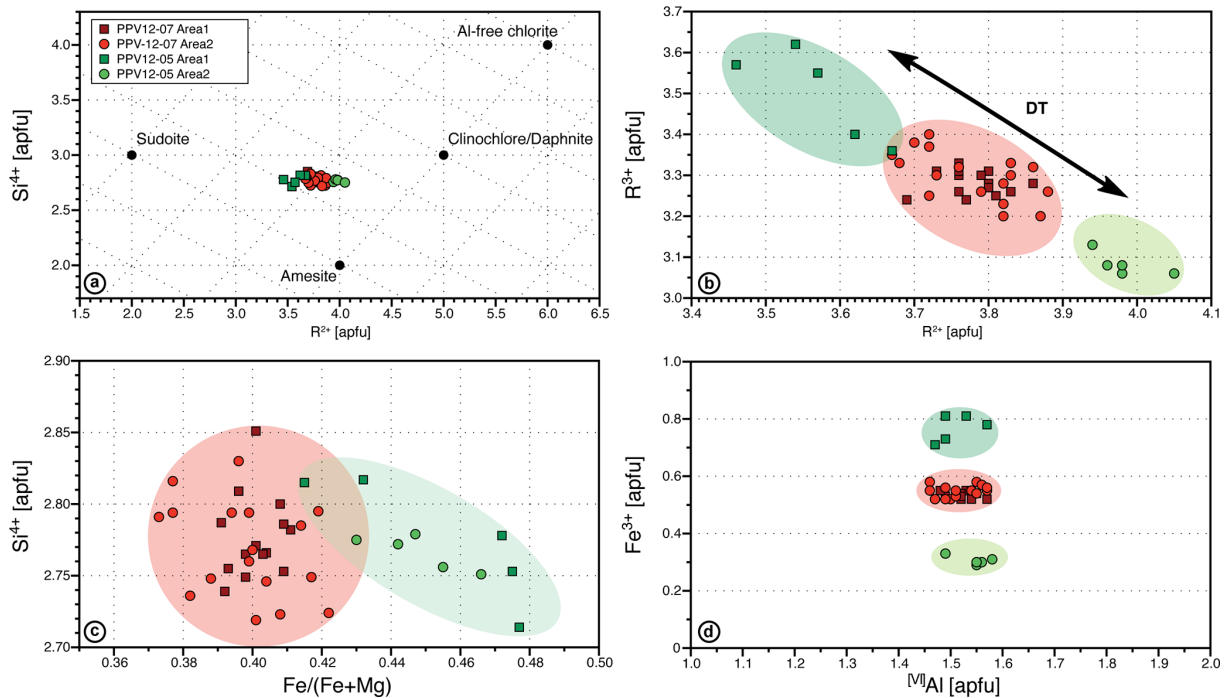

Figure 8. Structural formula values of synkinematic chlorite from the damage zone in red (sample PPV12-07) and from the core zone in green (sample PPV12-05), with squares for Area 1 and circles for Area 2 (cf. Figs. 5 and 6 for analyses location). The graphs show **(a)** Si vs. R^{2+}, **(b)** R^{3+} vs. R^{2+}, **(c)** Si vs. $Fe_{total}/(Fe_{total} + Mg)$, and **(d)** Fe^{3+} vs. $^{[VI]}Al$ diagrams. Note that R^{2+} refers to divalent cations (Fe^{2+} and Mg^{2+}), and R^{3+} refers to trivalent cations (Al^{3+}, Fe^{3+}). Fe is regarded as total iron, i.e. Fe^{2+} and Fe^{3+}. apfu is for atoms per formula unit; $^{[VI]}Al$ is for aluminium in octahedral sheets.

daphnite, sudoite, and amesite end-members (Fig. 8a) and is closer to clinochlore, daphnite, and sudoite compositions. The tetrahedral content does not vary. The only difference observed concerns the octahedral composition. Indeed, while the Si and ^{IV}Al contents are largely constant, R^{2+} varies

from 4 to 3.5 apfu (Fig. 8a and b). Chlorite from the damage zone shows intermediate values around 3.75 apfu, while chlorite from the core zone shows lower values (Area 1) or higher values (Area 2). The variation in R^{2+} is anticorrelated to the R^{3+} (from 3.1 to 3.6) content, showing a

di-trioctahedral substitution (DT). This DT can be related to the $Fe/(Fe + Mg)$ variation (Fig. 8c), as well as the XFe^{3+} variation, while Al remains constant (Fig. 8d).

Chlorite compositions from both areas of PPV12-07 (damage zone) are very homogeneous. Chlorite compositions from PPV12-05 are more Fe-rich than those from PPV12-07. A difference exists between Area 1 and Area 2. Chlorite from Area 1 contains more Fe^{3+}, and chlorite from Area 2 contains more Fe^{2+}.

4.4　Chlorite thermometry

The temperature conditions of chlorite formation for the four microstructural domains described above were estimated using the XFe^{3+} values determined by μ-XANES synchrotron analyses coupled with microprobe analyses.

The results obtained with the ChlMicaEqui program of Lanari et al. (2014a) are presented in column 1 of Table 1. In the damage zone sample (PPV12-07), chlorites in the releasing overstep of Area 1 and in the high-angle vein of Area 2 exhibit formation temperatures of 270 ± 26 and $282 \pm 39\,°C$, respectively. In the PPV12-05 core zone sample, the temperature of the formation of the chlorite of Area 1 and of Area 2 is 276 ± 44 and $274 \pm 14\,°C$, respectively.

Regarding the Inoue et al. (2009) calculation (Table 1, column 3), in the damage zone sample (PPV12-07), chlorite of Area 1 and of Area 2 presents a formation temperature of 282 ± 25 and $292 \pm 35\,°C$, respectively. In the PPV12-05 core zone sample, the temperature of formation of the chlorite of Area 1 is $278 \pm 30\,°C$; in the vein in Area 2, the mean calculated temperature is $294 \pm 19\,°C$. These values are much lower than the value obtained without considering the XFe^{3+} ratio (Table 1; column 2).

Temperatures estimated using Vidal et al. (2005) with fixed values of XFe^{3+} determined by μ-XANES are reported in column 6 of Table 1. In the damage zone sample (PPV12-07), chlorites of Area 1 and of Area 2 have a formation temperature of 283 ± 20 and $292 \pm 36\,°C$, respectively. In PPV12-05 core zone sample, the temperature of the formation of the chlorites of Area 1 and of Area 2 is 293 ± 41 and $274 \pm 11\,°C$, respectively. Those temperatures are, most of the time, slightly higher than the temperatures estimated when we let the model estimate the XFe^{3+} ratio. Indeed, for PPV12-07 in Area 1, PPV12-07 in Area 2, and PPV12-05 in Area 1, temperatures are underestimated by about $10\,°C$, whereas the model underestimates the XFe^{3+} ratio (0.25 instead of 0.31, 0.23 instead of 0.32, and 0.22 instead of 0.39). The temperature of the chlorite formation for PPV12-05 in Area 2 is equivalent to the XFe^{3+} ratio.

For each type of chlorite, the temperatures estimated by the three models considering the XFe^{3+} ratio are very similar. We therefore decided to plot the average values in Fig. 9a of the discussion part, with about $279\,°C$ for PPV12-07 in Area 1, $289\,°C$ for PPV12-07 in Area 2, $282\,°C$ for PPV12-05 in Area 1, and $281\,°C$ for PPV12-05 in Area 2.

5　Discussion

The compositional variation in phyllosilicate minerals in diagenetic and low-grade metamorphic rocks is controlled by pressure and temperature conditions, as well as bulk rock composition, fluid quantity and composition, and redox conditions. In this study, several compositional groups of chlorites were distinguished based on their $Fe_{total}/(Fe_{total} + Mg)$ and the XFe^{3+} ratios. These compositional groups are associated with specific structural locations in the samples. In the damage zone, chlorite shows a homogeneous composition, including the XFe^{3+} ratio. Two types of chlorite were observed in the core zone, with the first one in the interboudin domain and the second at the edge of the mylonitized quartz vein. Each type has different XFe^{3+} values, with higher values for chlorite in the interboudin domain and lower values for chlorite in the mylonitized shear band. Their $Fe/(Fe+Mg)$ ratios are similar but higher than those of the chlorite in the damage zone.

5.1　Temperature of chlorite formation: evidence of hydrothermal fluid circulation

The temperatures estimated by the three models that consider the XFe^{3+} ratio are very similar. The temperature of the formation calculated for the four types of chlorite does not vary and is slightly less than $300\,°C$ (between 280 and $290\,°C$) (Fig. 9a).

The temperature conditions calculated by Abd Elmola et al. (2017) are slightly lower at around $270\,°C$ in the damage zone. These temperatures were estimated using an optimized XFe^{3+} value (Lanari and Duesterhoeft, 2019). It can be observed that the XFe^{3+} values are always underestimated compared to those calculated by μ-XANES analyses, which can explain the underestimation of these calculated temperatures. This explanation is confirmed by the equivalent difference we observed between the Vidal et al. (2006) temperature calculations with optimized calculated XFe^{3+} values and with XFe^{3+} values determined by μ-XANES. Indeed, considering the XFe^{3+} ratio can reduce the R^{2+} occupancy and increase the number of octahedral vacancies (e.g. Vidal et al., 2005). As the octahedral vacancy is correlated with temperature (e.g. Lanari et al., 2014a), modifying the amount of Fe^{3+} can result in different estimated temperature. The temperature variation caused by the introduction of the Fe^{3+} content is different for each thermometer (e.g. Inoue et al., 2009, and references therein; Bourdelle et al., 2013; Vidal et al., 2016), as shown in Table 1. Considering the XFe^{3+} ratio allows an accurate temperature calculation.

The temperature range obtained by Trincal et al. (2015) in oscillatory zoned chlorites was wider (from 300 to $400\,°C$), and a relationship between the FeO and MgO content variation and temperature variation was noticed. In fact, the most iron-rich layers of the oscillatory zoned chlorites correspond to lower temperatures, and the most magnesium-rich layers
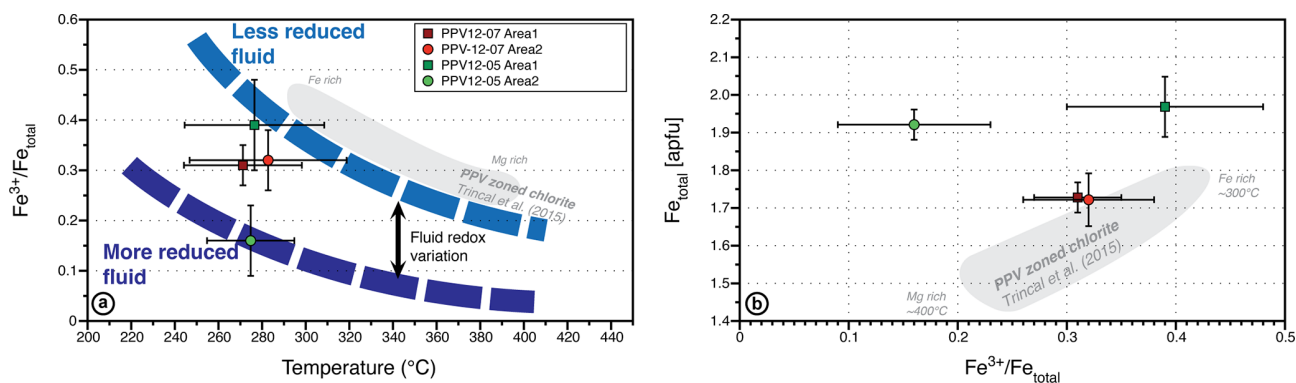
Figure 9. (a) XFe^{3+} (Fe^{3+}/Fe_{total}) vs. temperature. **(b)** Mean values of Fe_{total} vs. XFe^{3+} of the chlorite particles from the damage zone in red (PPV12-07) and from the core zone in green (PPV12-05), with circles for Area 1 and squares for Area 2 (cf. Figs. 5 and 6 for analyses location). Grey diamond shapes correspond to data from Trincal et al. (2015). apfu is for atoms per formula unit.

correspond to the higher ones. Compared to the results obtained in the present study, the iron-rich part of the oscillatory zoned chlorite broadly corresponds to the composition (Fig. 9b) and formation temperature (Fig. 9a) of homogenous chlorite localized in veins from the damage zone. On the other hand, regarding XFe^{3+} values, the magnesium-rich part of the oscillatory zoned chlorite is consistent with shear vein chlorite in the core zone, but it is different in the Fe–Mg composition and calculated temperature of crystallization. The higher temperature calculated for the magnesium-rich part of oscillatory zoned chlorite might be an artefact. It is likely that a local thermodynamic imbalance occurred during the crystallization of these layers.

In the case of homogeneous chlorites, the conditions of formation are slightly lower than 300 °C. This indicates a common thermal regime that favours formation under ductile/brittle conditions. The temperatures associated with chlorite formation, and hence fluid circulation in the PPVT fault, are slightly higher than those described in the central Pyrenees. Indeed, recent regional studies (e.g. Airaghi et al., 2020; Ducoux et al., 2021; Waldner et al., 2021; Labaume et al., 2016) have presented temperatures recorded during convergence that do not exceed 250 °C. Furthermore, in the Bielsa basement unit, close to the PPVT, shortening is accommodated by brittle and brittle–ductile shear zones active under temperatures around 250–300 °C, as indicated by the thermometric data on phyllosilicates and Raman spectrometry of carbonaceous material (Bellahsen et al., 2019). This could imply the circulation of a hot hydrothermal fluid in the PPVT fault zone, as suggested by Trincal et al. (2015).

5.2 Evolution of fluid–rock interactions in the PPVT fault zone

Even if the temperature variation is weak or negligible, mineralogical variations are observed. In fact, the damage and core zones have similar mineralogy with mainly K white mica, quartz, chlorite, calcite, minor rutile, and apatite. The

main differences are the absence of hematite in the core fault zone and an enrichment in phyllosilicate towards the latter. According to Abd Elmola et al. (2017) and Trincal et al. (2017), hematite dissolution and chlorite enrichment are responsible for the colour variation from red to green in the hanging wall. Furthermore, Abd Elmola et al. (2017) observed chemical variations; i.e. chlorite from the core zone contains more iron than chlorite from the damage zone (Figs. 8c and 9b). We can now add that, while the chlorite in the damage zone has a similar XFe^{3+} value, the chlorite in the core zone shows XFe^{3+} variations (Fig. 9). Indeed, the proportion of Fe^{3+} in chlorite at the edge of a V1 quartz vein (Area 2 in Fig. 9) is lower than in the damage zone, while the proportion of Fe^{3+} in chlorite in the interboudin domain (Area 1 in Fig. 9) is higher. The iron-rich layer of the oscillatory zoned chlorite corresponds to the homogenous composition of chlorite localized in the veins from the damage zone (Fig. 9). Moreover, the iron-rich layer of the oscillatory zoned chlorite is similar to the chlorite in the interboudin domain of the core zone in terms of XFe^{3+} values.

By synthesizing previous data with these new data, we can now have a global view of the reactions that took place in the PPVT fault zone. The PPVT fault, a second-order thrust associated with the major Gavarnie thrust, brought the Cretaceous limestone into contact with the Triassic sandstone and pelite at 36.9 ± 0.2 Ma (Abd Elmola et al., 2018). Fluids circulated along this interface (Fig. 10) and caused the formation of new phyllosilicates.

According to Grant (1989), fluids that circulated in the PPVT fault correspond to the mixing of mature-formation brines with a less concentrated fluid of probable meteoric origin. Indeed, recent studies (e.g. Barré et al., 2021; Cathelineau et al., 2021; Cruset et al., 2021; Ducoux et al., 2021) show that evaporitic-related fluids are ubiquitous throughout the geological history of the Pyrenees due to the presence of large amounts of Triassic evaporites (Labaume and Teixell, 2020) and the presence of evaporitic minerals in Lower Tri-

Table 1. Calculated temperatures obtained by the thermodynamical model developed by Lanari et al. (2014a) using the mean value of XFe^{3+} obtained by μ-XANES measurements: PPV12-07 in Area 1 with $XFe^{3+} = 0.31$, PPV12-07 in Area 2 with $XFe^{3+} = 0.32$, PPV12-05 in Area 1 with $XFe^{3+} = 0.39$, and PPV12-05 in Area 2 with $XFe^{3+} = 0.16$. Calculated temperatures were obtained by the semi-empirical thermometer developed by Inoue (Inoue et al., 2009) using (1) $Fe_{total} = Fe^{2+}$ and (2) the mean value of XFe^{3+} obtained by μ-XANES measurements. Calculated temperatures were obtained by the thermodynamical model developed by Vidal et al. (2005, 2006) using (3) the XFe calculated by the model for each chlorite composition and (2) the mean value of XFe^{3+} obtained by μ-XANES measurements.

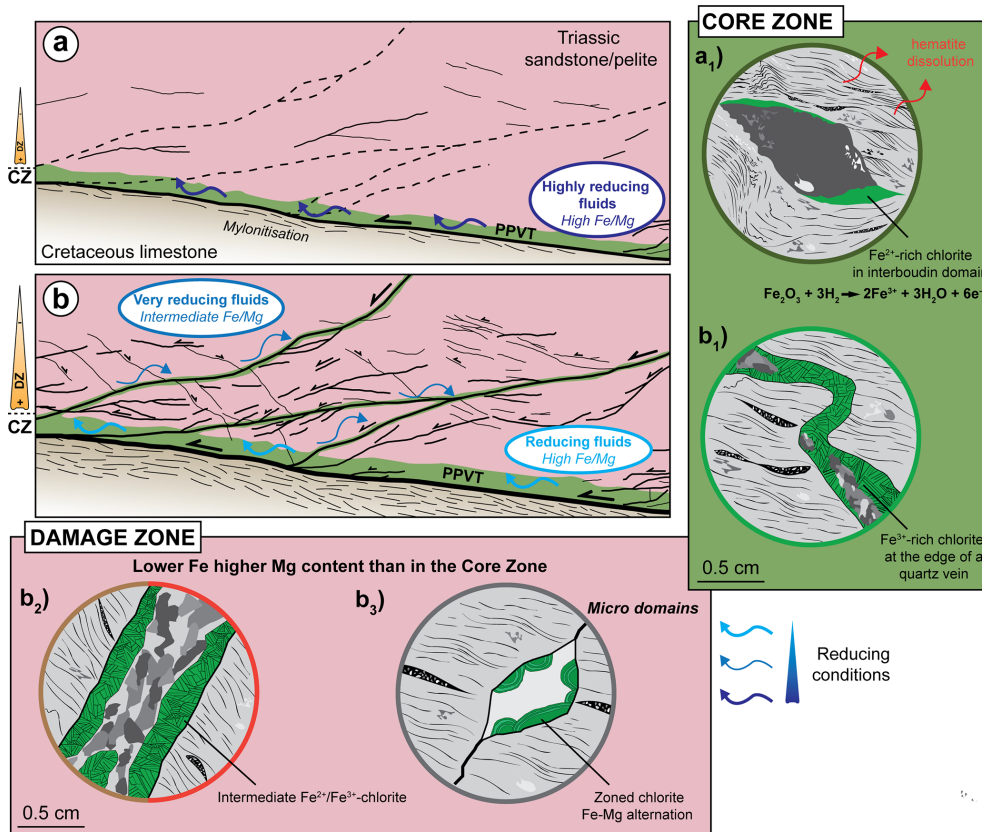|		Modelled temperature (°C) with Lanari et al. (2014a)	Modelled temperature (°C) with Inoue et al. (2009)		Modelled temperature (°C) and XFe with Vidal et al. (2006)		
		$XFe = \mu$-XANES values (2)	$Fe_{total} = Fe^{2+}$ (1)	$XFe = \mu$-XANES values (2)	Modelled XFe	$XFe =$ modelled values (3)	$XFe = \mu$-XANES values (2)
PPV12-07 (Area 1)	1	316	367	330	18	313	320
	2	261	312	276	25	266	272
	3	248	302	266	29	256	256
	4	283	344	306	24	288	289
	5	282	328	292	24	282	287
	6	256	300	264	25	261	266
	7	275	320	284	22	278	287
	8	288	326	290	20	286	300
	9	260	317	281	27	270	263
	10	296	339	303	19	297	311
	11	288	329	294	20	291	299
	12	242	292	257	32	250	250
	13	213	251	219	36	222	286
	14	276	329	293	24	282	281
Mean value		270	318	282	25	274	283
SD		26	27	26	5	23	20
PPV12-07 (Area 2)	1	257	316	281	30	268	268
	2	240	306	270	35	252	252
	3	251	295	260	27	258	258
	4	293	322	286	17	291	313
	5	317	360	324	17	313	327
	6	355	395	356	13	344	350
	7	288	352	314	23	290	300
	8	326	345	307	12	313	340
	9	311	377	339	21	312	316
	10	262	337	301	31	275	275
	11	255	314	277	28	265	260
	12	355	382	344	12	340	351
	13	274	322	285	22	279	287
	14	289	319	282	18	285	308
	15	226	271	237	34	235	235
	16	248	287	250	26	254	258
	17	254	289	253	24	259	270
Mean value		282	329	292	23	284	292
SD		39	36	35	7	31	36
PPV12-05 (Area 1)	1	343	367	316	10	321	353
	2	259	295	248	20	261	277
	3	242	314	267	32	254	270
	4	240	304	257	31	251	250
	5	295	355	303	18	291	313
Mean value		276	327	278	22	276	293
SD		44	32	30	9	30	41
PPV12-05 (Area 2)	1	277	311	290	17	275	275
	2	267	306	285	22	270	270
	3	261	302	280	22	263	263
	4	268	309	287	21	270	270
	5	298	352	328	19	292	292
Mean value		274	316	294	20	274	274
SD		14	20	19	2	11	11

Figure 10. Schematic PPVT fluid circulations and chemical transfers. **(a)** Percolation of a highly reducing fluid along the thrust fault leading to the dissolution of hematite and the crystallization of the Fe^{3+}-rich chlorite a_1. **(b)** Transformations of the initial fluid and circulation of the modified fluid leading to the crystallization of the elongated chlorite b_1 in the core zone and to the chlorites of the damage zone b_2 and b_3.

assic pelites. The resulting fluids are mixed in different proportions with more dilute water sources (e.g. meteoric water and seawater), thus resulting in inducing the recording of a relatively wide salinity range in the fluid inclusions. In our case, the fluids circulating at the interface between Cretaceous limestone and the Triassic pelite have the same brine signature but are more or less diluted (Grant, 1989). They were already enriched in magnesium because of their origin in the formation of brine but also because they reacted with the dolomitic mylonite of the footwall.

The fluid with a temperature of ~ 280–$290\,°C$ caused the dissolution of the hematite initially present in the core zone pelite (Fig. 10a). This dissolution enriched the brine in Fe^{3+}. Conditions were then favourable for the formation of Fe^{3+}-rich chlorite in the interboudin extensional domains crosscutting older V1 quartz veins (Fig. 10a$_1$). According to modelling performed by Abd Elmola et al. (2017), the redox condition for the precipitation of chlorite instead of other minerals after the dissolution of hematite should be highly reducing ($< -830\,mV$). The following reactions may have occurred:
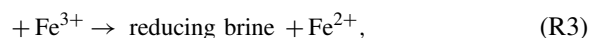
highly reducing brine

$$+ Fe_2O_3 \rightarrow \text{ highly reducing brine } + Fe^{3+}, \qquad (R1)$$

highly reducing brine
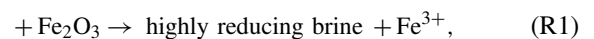
$$+ Fe^{3+} \rightarrow Fe^{3+}\text{–chlorite } + \text{ highly reducing brine.} \quad (R2)$$
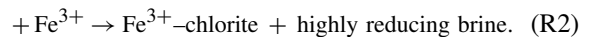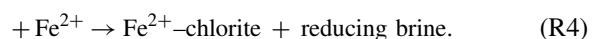
The presence of Fe^{3+}-rich chlorite is in good agreement with other studies showing that the incorporation of ferric iron into chlorite can be significant in a low-grade context (e.g. Beaufort et al., 1992; Inoue et al., 2009, and references therein).

In reducing conditions, some of the iron was reduced to Fe^{2+}, leading to the formation of another type of chlorite, the Fe^{2+}-rich chlorite at the edge of V1 quartz veins (Fig. 10b$_1$). The XFe^{3+} evolution is compatible with the decrease in oxygen fugacity buffered by the hematite–chlorite equilibrium:

highly reducing brine

$$+ Fe^{3+} \rightarrow \text{ reducing brine } + Fe^{2+}, \qquad (R3)$$

reducing brine

$$+ Fe^{2+} \rightarrow Fe^{2+}\text{–chlorite } + \text{ reducing brine.} \qquad (R4)$$

The two types of chlorite require different redox conditions. However, no evidence of successive precipitation was observed. The coexistence of both Fe^{3+}–chlorite and Fe^{2+}–chlorite could be explained by a successive precipitation from Reaction (2) and Reaction (4) but also by local reaction and disequilibrium.

In the damage zone, the chlorite from releasing oversteps along shear surfaces and the chlorite from veins cross-cutting the cleavage at high-angle are very similar in composition. This suggests that they are derived from the same process (Fig. 10b$_2$). Indeed, fluid expulsion from the core zone towards the damage zone was favoured by compactional deformation in the core zone, whereas extensional fractures are more developed in the damage zone, resulting in abundant vein precipitation along them.

The iron released by the dissolution of hematite in the core zone was partially re-incorporated into the synkinematic chlorites of the core zone since Fe is less mobile than Mg in this environment. This fluid was slightly depleted in iron, which explains why the chlorite in the damage zone has slightly lower Fe/(Fe+Mg) values. Following the precipitation of chlorite rich in Fe^{3+} and Fe^{2+} in the core zone, the fluid had a little less marked reducing budget. The chlorite of the damage zone therefore has intermediate XFe^{3+} values between those of the core zone.

As for the zoned chlorite, its zoning is rather due to local chemical variation. According to Trincal et al. (2015), the process of fault–valve behaviour with hot fluid pulses intercalated with cooling periods explains the crystallization of the zoning of chlorite. However, the zoning pattern could also occur with the circulation of a single fluid. Indeed, zoning of mineral compositions does not always reflect the evolution of fluid composition (Borg et al., 2014). These authors showed that during rapid fluid–rock reactions, ultra-local fluid composition variation can form complex mineral zoning patterns. In the case of PPVT fault, the iron-rich rims correspond to the homogeneous chlorite of the damage zone and are formed under the same conditions, whereas the magnesium-rich rims are related to ultra-local fluid variation. This scenario is consistent with the fact that FeO–MgO variation is not always closely related to temperature variations but sometimes to chemical variations (Chinchilla et al., 2016). At the outcrop scale, this observation is also consistent with the very localized fluid circulation along the faults and damage zone fractures (Fig. 2) and the lack of evidence for hydraulic overpressure (Smith et al., 2008; Masoch et al., 2019; Gosselin et al., 2020), a process commonly associated with fault valve mechanisms (Sibson, 1992; Cox, 2016; Zhu et al., 2020).

5.3   Implication for the fault-hosted geothermal systems

Differences in XFe^{3+} ratios in chlorite from the PPVT fault mark a redox evolution of the fluid associated with their formation (Fig. 9b). Similar temperatures between 280 and 290 °C, obtained for the different chlorite types (Fig. 9a), in-dicate a common thermal regime. The results obtained highlight different processes occurring in the fault zone; in the core zone, the hematite dissolution process is very efficient. It can be explained by the initiation of fluid circulation associated with the nucleation of the deformation at this rheological contact (Barnes et al., 2020; Fagereng and Beall, 2021). The significant permeability of the core zone can be explained by an increase in the permeability associated with the activation of the fault (Sibson, 2000; Caine et al., 2010; Cox et al., 2015) and/or a fault growth mechanism (e.g. Mitchell and Faulkner, 2009; Mayolle et al., 2019), suggesting a localized fluid flow near the fault contact prior to circulation throughout the fault zone. In the damage zone, the efficiency of redox processes appears to be largely controlled by the presence of the synthetic faults which form second-order structures and by hematite dissolution affecting lower volumes around these faults (Fig. 3). In this fault domain, fluid flow appears to be essentially driven by fracture networks and is also supported by the low permeability of the pelitic photolith (e.g. Neuzil, 2019). In this context, the deformation has a strong influence on the fluid pathways (e.g. Baker et al., 1989; Cox et al., 2015; Hobbs and Ord, 2018). This control by the fracture network can explain the heterogeneous permeability of the structures in the damage zone. The efficiency of the redox processes (chlorite with intermediate XFe^{3+}) may therefore be affected. Major changes in the fracture network could lead to the formation of isolated microdomains in which the chemistry of fluid can be locally changed to form zoned chlorite. Zoning could be due to cyclic chemical changes such as to crystal precipitation or local overpressure phenomena. The mineral-scale study of the PPVT fault zone demonstrates the importance of considering the fault zone as a whole to obtain a complete picture of the evolution of the associated fluids (Fig. 10).

Fault-hosted geothermal systems represent unconventional geothermal resources (e.g. Moeck, 2014; Duwiquet et al., 2022; Guillou-Frottier et al., 2024) with sufficient permeability due to limited stimulation or reactivation (e.g. Jolie et al., 2021). In this context, fractures, pressure, and fluid composition play a key role in the evolution of a geothermal system (Renard et al., 2000; Gudmundsson et al., 2001). Understanding the fracture pattern and associated alteration in the fault zone is of great importance for defining the geothermal potential as they are the essential part of the permeability in relatively impermeable protoliths (e.g. Ranjram et al., 2015). In an orogenic context, fractures and the alteration condition determine the entire fault-hosted geothermal system; i.e. (i) the infiltration of fluids, (ii) their circulation at depth and the size of the geothermal reservoir, and (iii) the location of fluid upwelling (e.g. Taillefer et al., 2017; Wanner et al., 2019). As observed along the Pyrenean thrusts (Fig. 1), the location of an active hydrothermal system is favoured by the superposition of deformation events along major faults, leading to an increase in fault zone permeability (e.g. Taillefer et al., 2021). In this context, the identification and char-

acterization of the first stage of the alteration associated with the Pyrenean thrusting is crucial for the geothermal exploration, as these permeable pathways can be (re-)used by the present-day hydrothermal system (e.g. Chauvet, 2019). The characterization of the natural hydrothermal circulation and the fracture network used by fluids is of great importance to adapt and limit the stimulation during the geothermal production (e.g. Gringarten et al., 1975; Breede et al., 2013).

6 Conclusions

Using the Pic de Port Vieux thrust fault as an example, we have investigated the main processes involved in the fluid circulation inside a fault zone. Speciation data obtained by X-ray absorption near-edge structure (XANES) spectroscopy combined with electron probe microanalysis (EPMA) closely linked to microstructural observations were used to constrain the conditions and evolution of fluid circulation in this orogenic context.

1. Microstructures associated with synkinematic minerals and detailed chlorite chemistry were investigated. The damage zone sample consists of a red pelitic matrix with two main generations of veins. Newly formed chlorite has been observed in quartz and chlorite veins associated with the extensional deformation of the schistosity, extensional openings corresponding to the boudinage of the veins of the first generation (chlorite of Area 1), or to releasing oversteps associated with shear surfaces that are extensional with respect to the schistosity (chlorite of Area 2). Chlorite shows a very homogeneous composition between clinochlore, daphnite, and sudoite endmember compositions. XFe^{3+} is of 32 %.

   The core zone sample, located a few centimetres away from the fault contact, consists of greenish pelite affected by a strongly developed schistosity. Synkinematic chlorites are found in the interboudin domain (Area 1) and at the edge of a V1 quartz vein (Area 2). They all contain more iron than the chlorites from the damage zone. The tetrahedral content of the two types of chlorite from the core zone is similar, but a ditrioctahedral substitution can be detected and related to XFe^{3+} variations. Chlorite located in the interboudin domain is closer to dioctahedral chlorite with XFe^{3+} of 39 %, whereas chlorite located at the edge of a V1 quartz vein is more trioctahedral with XFe^{3+} of 16 %.

2. As the amount of Fe^{3+} cations present in the crystal structure of chlorite has been quantified, the R^{2+} occupancy and the number of octahedral vacancies is more accurately determined. It allows precise chlorite crystallization temperatures to be calculated. All the results are about 280–290 °C, indicating a homogeneous crystallization temperature. This temperature could require the involvement of a hydrothermal fluid since temperatures

recorded during convergence in the central Pyrenees do not usually exceed 250 °C.

3. The petrographic observations and measured chemical compositions of the different chlorites can be explained by the circulation of an evaporite-related fluid. The redox process is the main process inducing the fluid evolution and mineral crystallization. It started with the hematite dissolution by a highly reductive fluid and continued with the crystallization of chlorite with various Mg/Fe and Fe^{3+}/Fe_{total} ratios in terms of their location and the reactions that previously modified the fluid composition and redox. The results obtained show that the hematite dissolution process is complete.

Thanks to this integrated study, we characterize the main processes related to the palaeo-fluid circulation within a fault zone. Micro-XANES spectroscopy provides unique insights regarding redox properties and their variation with time due to the mineral–fluid interactions – even at the scale of a fault zone. Moreover, iron state quantification is one of the weakest points of chlorite geothermometry that can be addressed by the methodology applied.

Author contributions. Conceptualization: DC, GM, PLab, AAE, MB, and MM. Fieldwork and sampling: PLab, AAE, and MB. Methodology and data acquisition: DC, GM, PLab, AAE, PLan, and MM. Data curation: DC, GM, PLab, PLan, and MM. Writing (original draft preparation): DC, GM, PLab, AAE, MB, and PLan. Writing (review and editing): DC and GM. Funding acquisition: DC, MB, and MM.

References

Abd Elmola, A., Charpentier, D., Buatier, M., Lanari, P., and Monié P.: Textural-chemical changes and deformation conditions registered by phyllosilicates in a fault zone (Pic de Port Vieux thrust, Pyrenees), Appl. Clay Sci., 144, 88–103, 2017.

Abd Elmola, A., Buatier, M., Monié, P., Labaume, P., Trap, P., and Charpentier, D.: ^{40}Ar/^{39}Ar muscovite dating of thrust activity: a case study from the Axial Zone of the Pyrenees, Tectonophysics, 745, 412–429, 2018.

Airaghi, L., Bellahsen, N., Dubacq, B., Chew, D., Rosenberg, C., Janots, E., Waldner, M., and Magnin, V.: Pre-orogenic upper crustal softening by lower greenschist facies metamorphic reactions in granites of the central Pyrenees, J. Metamorph. Geol., 38, 183–204, 2020.

Baker, E. T., Lavelle, J. W., Feely, R. A., Massoth, G. J., Walker, S. L., and Lupton, J. E.: Episodic venting of hydrothermal fluids from the Juan de Fuca Ridge, J. Geophys. Res.-Sol. Ea., 94, 9237–9250, https://doi.org/10.1029/JB094iB07p09237, 1989.

Barnes, P. M., Wallace, L. M., Saffer, D. M., and IODP Expedition 372 Scientists: Slow slip source characterized by lithological and geometric heterogeneity, Sci. Adv., 6, eaay3314, https://doi.org/10.1126/sciadv.aay3314, 2020.

Barnolas, A., Chiron, J. C., and Guérangé, B.: Synthèse géologique et géophysique des Pyrénées, Volume 1, Introduction, géophysique, cycle hercynien, BRGM, ISBN 2-7159-0797-4, 1996.

Barré, G., Fillon, C., Ducoux, M., Mouthereau, F., Gaucher, E. C., and Calassou, S.: The North Pyrenean Frontal Thrust: structure, timing and late fluid circulation inferred from seismic and thermal-geochemical analyses of well data, B. Soc. Geol. Fr.-Earth Sci. Bull., 192, 1–95, https://doi.org/10.1051/bsgf/2021046, 2021.

Barton, C. A., Zoback, M. D., and Moos, D.: Fluid flow along potentially active faults in crystalline rock, Geology, 23, 683, https://doi.org/10.1130/0091-7613(1995)023<0683:FFAPAF>2.3.CO;2, 1995.

Beaufort, D., Patrier, P., Meunier, A., and Ottaviani, M. M.: Chemical variations in assemblages including epidote and/or chlorite in the fossil hydrothermal system of Saint Martin (Lesser Antilles), J. Volcanol Geoth. Res., 51, 95–114., 1992.

Belgrano, T. M., Herwegh, M., and Berger, A.: Inherited structural controls on fault geometry, architecture and hydrothermal activity: An example from Grimsel Pass, Switzerland, Swiss J. Geosci., 109, 345–364, https://doi.org/10.1007/s00015-016-0212-9, 2016.

Bellahsen, N., Bayet, L., Denele, Y., Waldner, M., Airaghi, L., Rosenberg, C., Dubacq, B., Mouthereau, F., Bernet, M., Pik, R., Lahfid, A., and Vacherat, A.: Shortening of the axial zone, pyrenees: Shortening sequence, upper crustal mylonites and crustal strength, Tectonophysics, 766, 433–452, https://doi.org/10.1016/j.tecto.2019.06.002, 2019.

Bense, V. F., Gleeson, T., Loveless, S. E., Bour, O., and Scibek J.: Fault zone hydrogeology, Earth-Sci. Rev., 127, 171–192, 2013.

Berman, R. G.: Thermobarometry using multi-equilibrium calculations; a new technique, with petrological applications, Can. Mineral., 29, 833–855, 1991.

Borg, S., Liu, W., Pearce, M., Cleverley, J., and MacRae, C.: Complex mineral zoning patterns caused by ultra-local equilibrium at reaction interfaces, Geology, 42, 415–418, https://doi.org/10.1130/G35287.1, 2014.

Bourdelle, F.: Low-Temperature Chlorite Geothermometry and Related Recent Analytical Advances: A Review, Minerals, 11, 130, https://doi.org/10.3390/min11020130, 2021.

Bourdelle, F., Parra, T., Beyssac, O., Chopin, C., and Vidal, O.: Clay minerals thermometry: a comparative study based on high-spatial-resolution analyses of illite and chlorite in Gulf Coast sandstones (Texas, USA), Am. Mineral., 98, 914–926, 2013.

Breede, K., Dzebisashvili, K., Liu, X., and Falcone, G.: A systematic review of enhanced (or engineered) geothermal systems: past, present and future, Geotherm. Energy, 1, 1–27, https://doi.org/10.1186/2195-9706-1-4, 2013.

Bruhn, R. L., Parry, W. T., Yonkee, W. A., and Thompson, T.: Fracturing and hydrothermal alteration in normal fault zones, Pure Appl. Geophys., 142, 609–644, 1994.

Caine, J. S., Evans, J. P., and Forster, C. B.: Fault zone architecture and permeability structure, Geology, 24, 1025–1028, https://doi.org/10.1130/0091-7613(1996)024<1025:FZAAPS>2.3.CO;2, 1996.

Caine, J. S., Bruhn, R. L., and Forster, C. B.: Internal structure, fault rocks, and inferences regarding deformation, fluid flow, and mineralization in the seismogenic stillwater normal fault, dixie valley, nevada, J. Struct. Geol., 32, 1576–1589, 2010.

Cathelineau, M.: Cation site occupancy in chlorites and illites as a function of temperature, Clay Miner., 23, 471–485, 1988.

Cathelineau, M. and Nieva, D.: A chlorite solid solution geothermometer the Los Azufres (Mexico) geothermal system, Contrib. Mineral. Petrol., 91, 235–244, 1985.

Cathelineau, M., Boiron, M. C., and Jakomulski, H.: Triassic evaporites: A vast reservoir of brines mobilized successively during rifting and thrusting in the Pyrenees, J. Geol. Soc., 178, jgs20020-259, https://doi.org/10.1144/jgs2020-259, 2021.

Chauvet, A.: Structural control of ore deposits: The role of pre-existing structures on the formation of mineralised vein systems, Minerals, 9, 56, https://doi.org/10.3390/min9010056, 2019.

Chinchilla, D., Arroyo, X., Merinero, R., Piña, R., Nieto, F., Ortega, L., and Lunar, R.: Chlorite geothermometry applied to massive and oscillatory-zoned radiated Mn-rich chlorites in the Patricia Zn-Pb-Ag epithermal deposit (NE, Chile), Appl. Clay Sci., 134, 210–220, 2016.

Clauer, N., Rais, N., Schaltegger, U., and Piqué, A.: K-Ar systematics of clay-to-mica minerals in a multi-stage low-grade metamorphic evolution, Chem. Geol., 124, 305–316, https://doi.org/10.1016/0009-2541(95)00055-Q, 1995.

Cochelin, B., Chardon, D., Denèle, Y., Gumiaux, C., and Le Bayon, B.: Vertical strain partitioning in hot Variscan crust: Syn-convergence escape of the Pyrenees in the Iberian–Armorican syntax, B. Soc. Geol. Fr.-Earth Sci. Bull., 188, 39, https://doi.org/10.1051/bsgf/2017206, 2017.

Cox, S. C., Menzies, C. D., Sutherland, R., Denys, P. H., Chamberlain, C., and Teagle, D. A. H.: Changes in hot spring temperature and hydrogeology of the Alpine Fault hanging wall, New Zealand, induced by distal South Island earthquakes, Geofluids, 15, 216239, https://doi.org/10.1111/gfl.12093, 2015.

Cox, S. F.: Injection-driven swarm seismicity and permeability enhancement: Implications for the dynamics of hydrothermal ore systems in high fluid-flux, overpressured faulting regimes-An invited paper, Econ. Geol., 111, 559–587, https://doi.org/10.2113/econgeo.111.3.559, 2016.

Cruset, D., Vergés, J., Benedicto, A., Gomez-Rivas, E., Cantarero, I., John, C. M., and Travé, A.: Multiple fluid flow events from salt-related rifting to basin inversion (Upper Pedraforca thrust sheet, SE Pyrenees), Basin Res., 33, 3102–3136, https://doi.org/10.1111/bre.12596, 2021.

De Caritat, P., Hutcheon, I., and Walshe, J. L.: Chlorite geothermometry; a review, Clay. Clay Miner., 41, 219–239, 1993.

De Grave, E., Vandenbruwaene, J., and Bockstael, M. V.: ^{57}Fe Mössbauer spectroscopic analysis of chlorite, Phys. Chem. Miner., 15, 173–180, 1987.

Dewey, J. F.: Evolution of the Appalachian/Caledonian Orogen, Nature, 222, 124–129, https://doi.org/10.1038/222124a0, 1969.

Diamond, L. W., Wanner, C., and Waber, H. N.: Penetration depth of meteoric water in orogenic geothermal systems, Geology, 46, 1063–1066, https://doi.org/10.1130/G45394.1, 2018.

Dorsey, M. T., Rockwell, T. K., Girty, G. H., Ostermeijer, G. A., Browning, J., Mitchell, T. M., and Fletcher, J. M.: Evidence of hydrothermal fluid circulation driving elemental mass redistribution in an active fault zone, J. Struct. Geol., 144, 104269, https://doi.org/10.1016/j.jsg.2020.104269, 2021.

Ducoux, M., Jolivet, L., Masini, E., Augier, R., Lah, A., Bernet, M., and Calassou, S.: Distribution and intensity of High-Temperature Low-Pressure metamorphism across the Pyrenean–Cantabrian belt: constraints on the thermal record of the pre-orogenic hyperextension rifting, B. Soc. Geol. Fr.-Earth Sci. Bull., 192, 43, https://doi.org/10.1051/bsgf/2021029, 2021.

Duwiquet, H., Magri, F., Lopez, S., Guillon, T., Arbaret, L., Bellanger, M., and Guillou-Frottier, L.: Tectonic Regime as a Control Factor for Crustal Fault Zone (CFZ) Geothermal Reservoir in an Amagmatic System: A 3D Dynamic Numerical Modeling Approach, Nat. Resour., 31, 3155–3172, https://doi.org/10.1007/s11053-022-10116-w, 2022.

Eude. A., Soliva, R., Poprawski, Y., Frochot, A., Lacombe, S., and Grenier, M.: Contrôle tectonique des résurgences hydrothermales Pyrénéennes: implications géothermiques, in: 27e édition de la Réunion des Sciences de la Terre, https://www.researchgate.net/publication/344426890_Controle_tectonique_des_resurgences_hydrothermales_Pyreneennes_implications_geothermiques (last access: 25 August 2025), 2020.

Fagereng, Å. and Beall, A.: Is complex fault zone behaviour a reflection of rheological heterogeneity?, Philos. T. R. Soc. A, 379, 20190421, https://doi.org/10.1098/rsta.2019.0421, 2021.

Faulkner, D. R., Jackson, C. A. L., Lunn, R. J., Schlische, R. W., Shipton, Z. K., Wibberley, C. A. J., and Withjack, M. O.: A review of recent developments concerning the structure, mechanics and fluid flow properties of fault zones, J. Struct. Geol., 32, 1557–1575, https://doi.org/10.1016/j.jsg.2010.06.009, 2010.

Fossen, H. and Cavalcante, G. C. G.: Shear zones – A review, Earth-Sci. Rev., 171, 434–455, https://doi.org/10.1016/j.earscirev.2017.05.002, 2017.

Fossen, H., Cavalcante, G. C. G., Pinheiro, R. V. L., and Archanjo, C. J.: Deformation-progressive or multiphase?, J. Struct. Geol., 125, 82–99, 2019.

Fusseis, F. and Handy, M. R.: Micromechanisms of shear zone propagation at the brittle-viscous transition, J. Struct. Geol., 30, 1242-1253, https://doi.org/10.1016/j.jsg.2008.06.005, 2008.

Gosselin, J. M., Audet, P., Estève, C., McLellan, M., Mosher, S. G., and Shaeffer, A. J.: Seismic evidence for megathrust fault-valve behavior during episodic tremor and slip. Sci. Adv., 6, eaay5174, https://doi.org/10.1126/sciadv.aay5174, 2020.

Grant, N.: Deformation and fluid processes in thrust sheets from the central Pyrenees, Doctoral dissertation, University of Leeds, https://etheses.whiterose.ac.uk/2210/ (last access: 25 August 2025), 1989.

Grant, N.: Episodic discrete and distributed deformation: consequences and controls in a thrust culmination from the central Pyrenees, J. Struct. Geol., 12, 835–850, https://doi.org/10.1016/0191-8141(90)90058-7, 1990.

Grant, N.: Post-emplacement extension within a thrust sheet from the central Pyrenees, J. Geol. Soc. London, 149, 775–792, https://doi.org/10.1144/gsjgs.149.5.0775, 1992.

Grant, N., Banks, D. A., McCaig, A. M., and Yardley, B. W. D.: Chemistry, source, and behavior of fluids involved in alpine thrusting of the Central Pyrenees, J. Geophys. Res.-Sol. Ea., 95, 9123–9131, https://doi.org/10.1029/JB095iB06p09123, 1990.

Gringarten, A., Witherspoon, P., and Ohnishi, Y.: Theory of heat extraction from fractured hot dry rock, J. Geophys. Res., 80, 1120–1124, https://doi.org/10.1029/JB080i008p01120, 1975.

Gudmundsson, A., Berg, S. S., Lyslo, K. B., and Skurtveit, E.: Fracture networks and fluid transport in active fault zones, J. Struct. Geol., 23, 343–353, https://doi.org/10.1016/S0191-8141(00)00100-0, 2001.

Gueydan, F., Mehl, C., and Parra, T.: Stress-strain rate history of a midcrustal shear zone and the onset of brittle deformation inferred from quartz recrystallized grain size, Geol. Soc. Spec. Publ., 243, 127–142, https://doi.org/10.1144/GSL.SP.2005.243.01.10, 2005.

Guillou-Frottier, L., Milesi, G., Roche, V., Duwiquet, H., and Taillefer, A.: Heat flow, thermal anomalies, tectonic regimes and high-temperature geothermal systems in fault zones, C. R. Geosci., 356, 1–33, https://doi.org/10.5802/crgeos.213, 2024.

Hayes, J. B.: Polytypism of chlorite in sedimentary rocks, Clay. Clay Miner., 18, 285–306, 1970.

Hobbs, B. E. and Ord, A.: Episodic modes of operation in hydrothermal gold systems: Part II. A model for gold deposition, Geol. Soc. Spec. Pub., 453, 147–164, https://doi.org/10.1144/SP453.1, 2018.

Holm, D. K., Norris, R. J., and Craw, D.: Brittle and ductile deformation in a zone of rapid uplift: Central Southern Alps, New Zealand, Tectonics, 8, 153–168, https://doi.org/10.1029/TC008i002p00153, 1989.

Hueck, M., Wemmer, K., Basei, M. A. S., Philipp, R. P., Oriolo, S., Heidelbach, F., Oyhantçabal, P., and Siegesmund, S.: Dating recurrent shear zone activity and the transition from ductile to brittle deformation: White mica geochronology applied to the Neoproterozoic Dom Feliciano Belt in South Brazil, J. Struct. Geol., 141, 104199, https://doi.org/10.1016/j.jsg.2020.104199, 2020.

Incerpi, N., Manatschal, G., and Martire, L.: Characteristics and timing of hydrothermal fluid circulation in the fossil Pyrenean hyperextended rift system: new constraints from the Chaînons Béarnais (W Pyrenees), Int. J. Earth Sci. (Geol. Rundsch.), 109, 1071–1093, https://doi.org/10.1007/s00531-020-01852-6, 2020.

Inoue, A., Meunier, A., Patrier-Mas, P., Rigault, C., Beaufort, D., and Vieillard, P.: Application of chemical geothermometry to low-temperature trioctahedral chlorites, Clay. Clay Miner., 57, 371–382, 2009.

Jiménez, J., Gimeno, M. J., and Auqué, L. F.: Geochemical characterisation and modelling of the Luchon hydrothermal system (Central Pyrenees, France) and lessons learnt for the use of geochemical modelling techniques in granite-hosted alkaline thermal waters, Geothermics, 106, 102573, https://doi.org/10.1016/j.geothermics.2022.102573, 2022.

Jolie, E., Scott, S., Faulds, J., Chambefort, I., Axelsson, G., Gutierrez-Negrin, L. S., Regenspurg, S., Ziegler, M., Ayling, B., Richter, A., and Zemedkun, M. T.: Geological controls on geothermal resources for power generation, Nat. Rev. Earth Environ., 2, 324–339, https://doi.org/10.1038/s43017-021-00154-y, 2021.

Kirkland, C., Olierook, H. K. H., Danisik, M., Liebmann, J., Hollis, J., Ribeiro, B. V., and Rankenburg, K.: Dating mylonitic overprinting of ancient rocks, Communications Earth Environonment, 4, 47, https://doi.org/10.1038/s43247-023-00709-5, 2023.

Labaume, P. and Teixell, A.: Evolution of salt structures of the Pyrenean rift (Chaînons Béarnais, France): Form hyperextension to tectonic inversion, Tectonophysics, 785, 228451, https://doi.org/10.1016/j.tecto.2020.228451, 2020.

Labaume, P., Meresse, F., Jolivet, M., Teixell, A., and Lahfid, A.: Tectonothermal history of an exhumed thrust-sheet-top basin: an example from the south Pyrenean thrust belt, Tectonics, 35, 1280–1313, https://doi.org/10.1002/2016TC004192, 2016.

Lacroix, B., Charpentier, D., Buatier, M., Vennemann, T., Labaume, P., Adatte, T., Travé, A., and Dubois, M.: Formation of chlorite during thrust fault reactivation. Record of fluid origin and P-T conditions in the Monte Perdido thrust fault (southern Pyrenees), Contrib. Mineral. Petrol., 163, 1083–1102, 2012.

Lanari, P.: Micro-cartographie PT-e dans les roches métamorphiques. Applications aux Alpes et à l'Himalaya, Doctoral dissertation, Université de Grenoble, https://theses.hal.science/tel-00799283 (last access: 25 August 2025), 2012.

Lanari, P. and Duesterhoeft, E.: Modeling metamorphic rocks using equilibrium thermodynamics and internally consistent databases: Past achievements, problems and perspectives, J. Petrol., 60, 19–56. https://doi.org/10.1093/petrology/egy105, 2019.

Lanari, P., Vidal, O., De Andrade, V., Dubacq, B., Lewin, E., Grosch, E. G., and Schwartz, S.: XMapTools: A MATLAB©-based program for electron microprobe X-ray image processing and geothermobarometry, Comput. Geosci., 62, 227–240, 2014b.

Lanari, P., Wagner, T., and Vidal, O.: A thermodynamic model for di-trioctahedral chlorite from experimental and natural data in the system MgO-FeO-Al$_2$O$_3$- SiO$_2$-H$_2$O: applications to P-T sections and geothermometry, Contrib. Mineral. Petrol., 167, 1–19, 2014a.

Luijendijk, E., Winter, T., Köhler, S., Ferguson, G., Hagke, C., and Scibek, J.: Using Thermal Springs to Quantify Deep Groundwater Flow and Its Thermal Footprint in the Alps and a Comparison With North American Orogens, Geophys. Res. Lett., 47, e2020GL090134, https://doi.org/10.1029/2020GL090134, 2020.

Masci, L., Dubacq, B., Verlaguet, A., Chopin, C., Andrade, V. D., and Herviou, C.: A XANES and EPMA study of Fe3+ in chlorite: Importance of oxychlorite and implications for cation site distribution and thermobarometry, Am. Mineral., 104, 403–417, https://doi.org/10.2138/am-2019-6766, 2019.

Masoch, S., Fondriest, M., Preto, N., Secco, M., and Di Toro, G.: Seismic cycle recorded in cockade-bearing faults (Col de Teghime, Alpine Corsica), J. Struct. Geol., 129, 103889, https://doi.org/10.1016/j.jsg.2019.103889, 2019.

Mathon, O., Beteva, A., Borrel, J., Bugnazet, D., Gatla, S., Hino, R., Kantor, I., Mairs, T., Muñoz, M., Pasternak, S., Perrin, F., and Pascarelli, S.: The Time resolved and Extreme conditions XAS (TEXAS) facility at the European Synchrotron Radiation Facility: the general purpose EXAFS bending magnet beamline BM23, J. Synchrotron Radiat., 22, 1548–1554, 2015.

Mayolle, S., Soliva, R., Caniven, Y., Wibberley, C., Ballas, G., Milesi, G., and Dominguez, S.: Scaling of fault damage zones in carbonate rocks, J. Struct. Geol., 124, 35–50, https://doi.org/10.1016/j.jsg.2019.03.007, 2019.

McCaig, A. M., Wayne, D. M., Marshall, J. D., Banks, D., and Henderson, I.: Isotopic and fluid inclusion studies of fluid movement along the Gavarnie Thrust, central Pyrenees; reaction fronts in carbonate mylonites, Am. J. Sci., 295, 309–343, 1995.

McCaig, A. M., Tritlla, J., and Banks, D. A.: Fluid mixing and recycling during Pyrenean thrusting: Evidence from fluid inclusion halogen ratios, Geochim. Cosmochim. Ac., 64, 3395–3412, https://doi.org/10.1016/S0016-7037(00)00437-3, 2000.

Medici, G., Ling, F., and Shang, J.: Review of discrete fracture network characterization for geothermal energy extraction, Front. Earth Sci., 11, 1328397, https://doi.org/10.3389/feart.2023.1328397, 2023.

Milesi, G., Monié, P., Münch, P., Soliva, R., Taillefer, A., Bruguier, O., Bellanger, M., Bonno, M., and Martin, C.: Tracking geothermal anomalies along a crustal fault using (U – Th)/He apatite thermochronology and rare-earth element (REE) analyses: the example of the Têt fault (Pyrenees, France), Solid Earth, 11, 1747–1771, https://doi.org/10.5194/se-11-1747-2020, 2020.

Mitchell, T. M. and Faulkner, D. R.: The nature and origin of off-fault damage surrounding strike-slip fault zones with a wide range of displacements: A field study from the Atacama fault system, northern Chile, J. Struct. Geol., 31, 802–816, https://doi.org/10.1016/j.jsg.2009.05.002, 2009.

Mitra, G.: Brittle to ductile transition due to large strains along the White Rock thrust, Wind River mountains, Wyoming, J. Struct. Geol., 6, 51–61, https://doi.org/10.1016/0191-8141(84)90083-X, 1984.

Moeck, I. S.: Catalog of geothermal play types based on geologic controls, Renew. Sust. Energ. Rev., 37, 867–882, https://doi.org/10.1016/j.rser.2014.05.032, 2014.

Monié, P., Münch, P., Milesi, G., Bonno, M., and Iemmolo, A.: $^{40}Ar/^{39}Ar$ geochronology of crustal deformation. C. R. Geosci., 356, 1–29, https://doi.org/10.5802/crgeos.209, 2024.

Montemagni, C. and Villa, I. M.: Geochronology of Himalayan shear zones: Unravelling the timing of thrusting from structurally complex fault rocks, J. Geol. Soc., 178, jgs2020-235, https://doi.org/10.1144/jgs2020-235, 2021.

Morton, N., Girty, G. H., and Rockwell, T. K.: Fault zone architecture of the San Jacinto fault zone in Horse Canyon, southern California: A model for focused post-seismic fluid flow and heat transfer in the shallow crust, Earth Planet. Sc. Lett., 329–330, 71–83, https://doi.org/10.1016/j.epsl.2012.02.013, 2012.

Mouthereau, F., Filleaudeau, P. Y., Vacherat, A., Pik, R., Lacombe, O., Fellin, M. G., Castelltort, S., Christophoul, F., and Masini, E.: Placing limits to shortening evolution in the Pyrenees: Role of margin architecture and implications for the Iberia/Europe convergence: Plate convergence in the Pyrenees, Tectonics, 33, 2283–2314, https://doi.org/10.1002/2014TC003663, 2014.

Müller, W.: Strengthening the link between geochronology, textures and petrology, Earth Planet. Sc. Lett., 206, 237–251, https://doi.org/10.1016/S0012-821X(02)01007-5, 2003.

Muñoz, J. A.:. Evolution of a continental collision belt: ECORS-Pyrenees crustal balanced cross-section. In Thrust tectonics, Dordrecht, Springer Netherlands, 235–246, https://doi.org/10.1007/978-94-011-3066-0_21, 1992.

Muñoz, M., De Andrade, V., Vidal, O., Lewin, E., Pascarelli, S., and Susini, J.: Redox and speciation micromapping using dispersive X-ray absorption spectroscopy: Application to iron chlorite mineral of a metamorphic rock thin section, Geochem. Geophy. Geosy., 7, Q11020, https://doi.org/10.1029/2006GC001381, 2006.

Muñoz, M., Vidal, O., Marcaillou, C., Pascarelli, S., Mathon, O., and Farges, F.: Iron oxidation state in phyllosilicate single crystals using Fe-K pre-edge and XANES spectroscopy: Effects of the linear polarization of the synchrotron X-ray beam, Am. Mineral., 98, 1187–1197, 2013.

Muñoz-López, D., Alías, G., Cruset, D., Cantarero, I., John, C. M., and Travé, A.: Influence of basement rocks on fluid evolution during multiphase deformation: the example of the Estamariu thrust in the Pyrenean Axial Zone, Solid Earth, 11, 2257–2281, https://doi.org/10.5194/se-11-2257-2020, 2020.

Neuzil, C. E.: Permeability of clays and shales, Annu. Rev. Earth Pl. Sc., 47, 247–273, https://doi.org/10.1146/annurev-earth-053018-060437, 2019.

Oriolo, S., Wemmer, K., Oyhantçabal, P., Fossen, H., Schulz, B., and Siegesmund, S.: Geochronology of shear zones – A review, Earth-Sci. Rev., 185, 665–683, https://doi.org/10.1016/j.earscirev.2018.07.007, 2018.

Parry, W. T., Hedderly-Smith, D., and Bruhn, R. L.: Fluid inclusions and hydrothermal alteration on the Dixie Valley Fault, Nevada, J. Geophys. Res.-Sol. Ea., 96, 19733–19748, https://doi.org/10.1029/91JB01965, 1991.

Perret, J., Eglinger, A., André-Mayer, A. S., Aillères, L., Feneyrol, J., Hartshorne, C., Abanyin, E., and Bosc, R.: Subvertical, linear and progressive deformation related to gold mineralization at the Galat Sufar South deposit, Nubian Shield, NE Sudan, J. Struct.

Geol., 135, 104032, https://doi.org/10.1016/j.jsg.2020.104032, 2020.

Pfalzer, P., Urbach, J. P., Klemm, M., and Horn, S.: Elimination of self-absorption in fluorescence hard-X-ray absorption spectra, Phys. Rev. B, 60, 9335–9339, 1999.

Rahl, J. M., Haines, S. H., and van der Pluijm, B. A.: Links between orogenic wedge deformation and erosional exhumation: evidence from illite age analysis of fault rock and detrital thermochronology of syn-tectonic conglomerates in the Spanish Pyrenees, Earth Planet. Sc. Lett., 307, 180–190, https://doi.org/10.1016/j.epsl.2011.04.036, 2011.

Ranjram, M., Gleeson, T., and Luijendijk, E.: Is the permeability of crystalline rock in the shallow crust related to depth, lithology or tectonic setting?, Geofluids, 15, 106–119, https://doi.org/10.1111/gfl.12098, 2015.

Renard, F., Gratier, J. P., and Jamtveit, B.: Kinetics of crack-sealing, intergranular pressure solution, and compaction around active faults, J. Struct. Geol., 22, 1395–1407, https://doi.org/10.1016/S0191-8141(00)00064-X, 2000.

Rolland, Y., Cox, S. F., and Corsini, M.: Constraining deformation stages in brittle-ductile shear zones from combined field mapping and 40Ar/39Ar dating: The structural evolution of the Grimsel Pass area (Aar Massif, Swiss Alps), J. Struct. Geol., 31, 1377–1394, https://doi.org/10.1016/j.jsg.2009.08.003, 2009.

Roure, F., Choukroune, P., Berastegui, X., Munoz, J. A., Villien, A., Matheron, P., Bareyt, M., Seguret, M., Camara, P., and Deramond, J.: Ecors deep seismic data and balanced cross sections: Geometric constraints on the evolution of the Pyrenees, Tectonics, 8, 41–50, https://doi.org/10.1029/TC008i001p00041, 1989.

Shata, S. and Hesse, R.: A refined XRD method for the determination of chlorite composition and application to the McGerrigle Mountains anchizone in the Quebec Appalachians, Can. Mineral., 36, 1525–1546, 1998.

Sibson, R. H.: Implications of fault-valve behaviour for rupture nucleation and recurrence, in: Earthquake Source Physics and Earthquake Precursors, edited by: Mikumo, T., Aki, K., Ohnaka, M., Ruff, L. J., and Spudich, P. K. P., Tectonophysics, 211, 283–293, 1992.

Sibson, R. H.: Fluid involvement in normal faulting, J. Geodyn., 29, 469–499, https://doi.org/10.1016/S0264-3707(99)00042-3, 2000.

Smith, S. A. F., Collettini, C., and Holdsworth, R. E.: Recognizing the seismic cycle along ancient faults: CO_2-induced fluidization of breccias in the footwall of a sealing low-angle normal fault, J. Struct. Geol., 30, 1034–1046, 2008.

Stierman, D. J.: Geophysical and geological evidence for fracturing, water circulation and chemical alteration in granitic rocks adjacent to major strike-slip faults. J. Geophys. Res.-Sol. Ea., 89, 5849–5857, https://doi.org/10.1029/JB089iB07p05849, 1984.

Taillefer, A., Soliva, R., Guillou-Frottier, L., Le Goff, E., Martin, G., and Seranne, M.: Fault-Related Controls on Upward Hydrothermal Flow: An Integrated Geological Study of the Têt Fault System, Eastern Pyrénées (France), Geofluids, 2017, 8190109, https://doi.org/10.1155/2017/8190109, 2017.

Taillefer, A., Guillou-Frottier, L., Soliva, R., Magri, F., Lopez, S., Courrioux, G., Millot, R., Ladouche, B., and Le Goff, E.: Topographic and Faults Control of Hydrothermal Circulation Along Dormant Faults in an Orogen, Geochem. Geophy. Geosy., 19, 4972–4995, https://doi.org/10.1029/2018GC007965, 2018.

Taillefer, A., Milesi, G., Soliva, R., Monnier, L., Delorme, P., Guillou-Frottier, L., and Le Goff, E.: Polyphased brittle deformation around a crustal fault: A multi-scale approach based on remote sensing and field data on the mountains surrounding the Têt hydrothermal system (Eastern Pyrénées, France), Tectonophysics, 804, 228710, https://doi.org/10.1016/j.tecto.2020.228710, 2021.

Tamburello, G., Chiodini, G., Ciotoli, G., Procesi, M., Rouwet, D., Sandri, L., Carbonara, N., and Masciantonio, C.: Global thermal spring distribution and relationship to endogenous and exogenous factors, Nat. Commun., 13, 6378, https://doi.org/10.1038/s41467-022-34115-w, 2022.

Tartaglia, G., Viola, G., van der Lelij, R., Scheiber, T., Ceccato, A., and Schönenberger, J.: "Brittle structural facies" analysis: A diagnostic method to unravel and date multiple slip events of long-lived faults, Earth Planet. Sc. Lett., 545, 116420, https://doi.org/10.1016/j.epsl.2020.116420, 2020.

Teixell, A.: The Ansó transect of the southern Pyrenees: basement and cover thrust geometries, J. Geol. Soc. London, 153, 301–310, 1996.

Teixell, A., Labaume, P., Ayarza, P., Espurt, N., De Saint Blanquat, M., and Lagabrielle, Y.: Crustal structure and evolution of the Pyrenean-Cantabrian belt: a review and new interpretations from recent concepts and data, Tectonophysics, 724–725, 146–170, https://doi.org/10.1016/j.tecto.2018.01.009, 2018.

Trincal, V., Lanari, P., Buatier, M., Lacroix, B., Charpentier, D., Labaume, P., and Munoz, M.: Temperature micro-mapping in oscillatory-zoned chlorite: Application to study of a green-schist facies fault zone in the Pyrenean Axial Zone (Spain), Am. Mineral., 100, 2468–2483, 2015.

Trincal, V., Buatier, M., Charpentier, D., Lacroix, B., Lanari, P., Labaume, P., Lahfid, A., and Vennemann, T.: Fluid-rock interactions related to metamorphic reducing fluid flow in meta-sediments: example of the Pic-de-Port-Vieux thrust (Pyrenees, Spain), Contrib. Mineral. Petrol., 172, 78, https://doi.org/10.1007/s00410-017-1394-5, 2017.

Trittla, J., Alonso Azcarate, J., Bottrell, S. H.: Molten sulphur-dominated fluids in the origin of a native sulphur mineralization in lacustrine evaporites from Cervera del Rio Alhama (Cameros Basin, NE Spain), J. Geochem. Explor., 69, 183–187, https://doi.org/10.1016/S0375-6742(00)00023-6, 2000.

van der Pluijm, B. A., Hall, C. M., Vrolijk, P. J., Pevear, D. R., and Covey, M. C.: The dating of shallow faults in the Earth's crust, Nature, 412, 172–175, https://doi.org/10.1038/35084053, 2001.

Vasseur, G., Gable, R., Feuga, B., and Bienfait, G.: Groundwater flow and heat flow in an area of mineral springs, Geothermics, 20, 99–117, https://doi.org/10.1016/0375-6505(91)90009-K, 1991.

Vergés, J., Fernàndez, M., and Martìnez, A.: The Pyrenean orogen: Pre-, syn-, and post-collisional evolution, J. Virtual Explor., 8, 55–74, https://doi.org/10.3809/jvirtex.2002.00058, 2002.

Vidal, O., Parra, T.and Trotet, F.: A thermodynamic model for Fe-Mg aluminous chlorite using data from phase equilibrium experiments and natural pelitic assemblages in the 100° to 600°C, 1 to 25 Kb range, Am. J. Sci., 301, 557–592, https://doi.org/10.2475/ajs.301.6.557, 2001.

Vidal, O., Parra, T., and Vieillard, P.: Thermodynamic properties of the Tschermak solid solution in Fe-chlorite: application to natural examples and possible role of oxidation, Am. Mineral., 90, 347–358, 2005.

Vidal, O., De Andrade, V., Lewin, E., Munoz, M., Parra, T., and Pascarelli, S.: P-T deformation-Fe^{3+}/Fe^{2+} mapping at the thin section scale and comparison with XANES mapping: application to a garnet-bearing metapelite from the Sambagawa metamorphic belt (Japan), J. Metamorph. Geol., 24, 669–683, 2006.

Vidal, O., Lanari, P., Munoz, M., Bourdelle, F., and De Andrade, V.: Deciphering temperature, pressure and oxygen-activity conditions of chlorite formation, Clay Miner., 51, 615–633, 2016.

Villa, I. M.: Dating deformation: The role of atomic-scale processes, J. Geol. Soc. London, 179, jgs2021-098, https://doi.org/10.1144/jgs2021-098, 2022.

Vissers, R. L. M., Ganerød, M., Pennock, G. M., and van Hinsbergen, D. J. J.: Eocene seismogenic reactivation of a Jurassic ductile shear zone at Cap de Creus, Pyrenees, NE Spain, J. Struct. Geol., 134, 103994, https://doi.org/10.1016/j.jsg.2020.103994, 2020.

Waldner, M., Bellahsen, N., Mouthereau, F., Bernet, M., Pik, R., Rosenberg, L., and Balvay, M.: Central Pyrenees Mountain Building: Constraints From New LT Thermochronological Data From the Axial Zone, Tectonics, 40, 289–302, https://doi.org/10.1029/2020TC006614, 2021.

Walker, J. R.: Chlorite polytype geothermometry, Clay. Clay Miner., 41, 260–267, 1993.

Wanner, C., Diamond, L. W., and Alt-Epping, P.: Quantification of 3-D thermal anomalies from surface observations of an orogenic geothermal system (Grimsel Pass, Swiss Alps), J. Geophys. Res.-Sol. Ea., 124, 10839–10854, https://doi.org/10.1029/2019JB018335, 2019.

Wanner, C., Waber, H. N., and Bucher, K.: Geochemical evidence for regional and long-term topography-driven groundwater flow in an orogenic crystalline basement (Aar Massif, Switzerland), J. Hydrol., 581, 124374, https://doi.org/10.1016/j.jhydrol.2019.124374, 2020.

Wilke, M., Farges, F., Petit, P. E., Brown, G. E., and Martin, F.: Oxidation state and coordination of Fe in minerals: An Fe K-XANES spectroscopic study, Am. Mineral., 86, 714–730, 2001.

Wiprut, D. and Zoback, M. D.: Fault reactivation and fluid flow along a previously dormant normal fault in the northern North Sea, Geology, 28, 595–598, https://doi.org/10.1130/0091-7613(2000)28<595:FRAFFA>2.0.CO;2, 2000.

Yin, A. and Harrison, T. M.: Geologic Evolution of the Himalayan-Tibetan Orogen, Annu. Rev. Earth Pl. Sc., 28, 211–280, https://doi.org/10.1146/annurev.earth.28.1.211, 2000.

Zane, A., Sassi, R., and Guidotti, C. V.: New data on metamorphic chlorite as a petrogenetic indicator mineral, with special regard to greenschist-facies rocks, Can. Mineral., 36, 713–726, 1998.

Zhu, W., Allison, K. L., Dunham, E. M., and Yang, Y.: Fault valving and pore pressure evolution in simulations of earthquake sequences and aseismic slip, Nat. Commun., 11, 4833, https://doi.org/10.1038/s41467-020-18598-z, 2020.